Top-of-Atmosphere Direct Radiative Effect of Aerosols over Global Oceans from Merged CERES and MODIS Observations

NORMAN G. LOEB

Center for Atmospheric Sciences, Hampton University, Hampton, Virginia

NATIVIDAD MANALO-SMITH

Analytical Services and Materials, Hampton, Virginia

(Manuscript received 17 December 2004, in final form 28 March 2005)

ABSTRACT

The direct radiative effect of aerosols (DREA) is defined as the difference between radiative fluxes in the absence and presence of aerosols. In this study, the direct radiative effect of aerosols is estimated for 46 months (March 2000–December 2003) of merged Clouds and the Earth's Radiant Energy System (CERES) and Moderate Resolution Imaging Spectroradiometer (MODIS) *Terra* global measurements over ocean. This analysis includes the contribution from clear regions in both clear and partly cloudy CERES footprints. MODIS–CERES narrow-to-broadband regressions are developed to convert clear-sky MODIS narrowband radiances to broadband shortwave (SW) radiances, and CERES clear-sky angular distribution models (ADMs) are used to estimate the corresponding top-of-atmosphere (TOA) radiative fluxes that are needed to determine the DREA. Clear-sky MODIS pixels are identified using two independent cloud masks: (i) the NOAA/National Environmental Satellite, Data, and Information Service (NESDIS) algorithm that is used for inferring aerosol properties from MODIS on the CERES Single Scanner Footprint TOA/Surface Fluxes and Clouds (SSF) product (NOAA SSF); and (ii) the standard algorithm that is used by the MODIS aerosol group to produce the MODIS aerosol product (MOD04). Over global oceans, direct radiative cooling by aerosols for clear scenes that are identified from MOD04 is estimated to be 40% larger than for clear scenes from NOAA SSF (5.5 compared to 3.8 W m^{-2}). Regionally, differences are largest in areas that are affected by dust aerosol, such as oceanic regions that are adjacent to the Sahara and Saudi Arabian deserts, and in northern Pacific Ocean regions that are influenced by dust transported from Asia. The net total-sky (clear and cloudy) DREA is negative (cooling) and is estimated to be -2.0 W m^{-2} from MOD04, and -1.6 W m^{-2} from NOAA SSF. The DREA is shown to have pronounced seasonal cycles in the Northern Hemisphere and large year-to-year fluctuations near deserts. However, no systematic trend in deseasonalized anomalies of the DREA is observed over the 46-month time series that is considered.

1. Introduction

Determination of the effects of aerosols on climate requires the use of chemical transport, radiation, and general circulation models. The models must be able to characterize the abundance, physical, chemical, and optical properties of aerosols with sufficient accuracy to determine aerosol direct radiative forcing to within a few tenths of a watts per squared meter Not surprisingly, the uncertainty in aerosol radiative forcing, as determined by comparisons between various climate models, is as large as the forcing itself (Houghton et al. 2001). To constrain the models and identify their strengths and weaknesses, the models need to be evaluated against surface, aircraft, and satellite observations (Haywood et al. 1999; Kinne et al. 2003). Because aerosol–climate interactions are complex, information from a wide array of observational and theoretical approaches is needed, and must be integrated and interpreted in a systematic manner (Diner et al. 2004).

A useful test of the models is to compare model and satellite estimates of the top-of-atmosphere (TOA) direct radiative effect of aerosols (DREA), defined as the difference between TOA radiative fluxes in the absence and presence of aerosols. In this context, the DREA refers to the total (natural and anthropogenic) direct

Corresponding author address: Dr. Norman G. Loeb, Mail Stop 420, NASA Langley Research Center, Hampton, VA 23681-2199.
E-mail: n.g.loeb@larc.nasa.gov

effect of aerosols on TOA radiative fluxes. DREA depends upon the cumulative effects of the aerosol type, amount, and optical properties over broad spectral intervals. Previous studies have used both narrowband and broadband satellite measurements to estimate the DREA. Boucher and Tanré (2000) inferred the DREA from narrowband Polarization and Directionality of the Earth's Reflectances (POLDER) measurements, and Chou et al. (2002) used measurements from the Sea-Viewing Wide Field-of-View Sensor (SeaWiFS) instrument. Broadband instruments, such as the Earth Radiation Budget Experiment (ERBE) and the Clouds and the Earth's Radiant Energy System (CERES), have also provided useful DREA estimates (e.g., Haywood et al. 1999; Satheesh et al. 1999; Christopher et al. 2000; Li et al. 2000; Loeb and Kato 2002; Weaver et al. 2002).

One advantage of using instruments such as ERBE or CERES to estimate the DREA is that the measurements are acquired over broad spectral intervals in the shortwave (SW) and terrestrial-infrared or longwave (LW) regions, so there is no need to use models to estimate the wavelength dependence of aerosol properties to infer the DREA. However, a limitation of these instruments is their coarse spatial resolution. Previous studies of the DREA from ERBE and CERES restricted the analysis to cloud-free footprints [10 km at nadir for the CERES Tropical Rainfall Measuring Mission (TRMM) satellite, 20 km for CERES *Terra*, 40 km for ERBE], thereby excluding aerosol contributions in partly cloudy scenes. As a result, the DREA is representative of only large-scale clear-sky meteorological conditions and regions. In this study, we introduce a new approach to overcome this limitation by exploiting the synergy between CERES and Moderate Resolution Imaging Spectroradiometer (MODIS) measurements on *Terra* to account for the SW DREA at sub-CERES footprint scales. MODIS–CERES narrow-to-broadband regressions are developed to convert clear-sky MODIS narrowband radiances to broadband SW radiances, and CERES clear-sky angular distribution models (ADMs) (Loeb et al. 2005) are used to estimate the corresponding TOA radiative fluxes that are needed to determine the DREA. The clear-sky MODIS radiances in this analysis are the same as those that are used to infer aerosol properties in two operational products that are provided by the CERES science team and the MODIS atmospheres group.

In the following sections, the methodology that is used to determine the DREA is described in detail, together with results that (i) investigate the sensitivity of the SW DREA to uncertainties in the identification of cloud-free MODIS pixels (i.e., cloud mask), (ii) examine the seasonal and interannual variability of the DREA, and (iii) estimate the total-sky (clear and cloudy) SW and net DREA (sum of SW and LW DREA).

2. Observations

The *Terra* spacecraft was launched on 18 December 1999 in a descending sun-synchronous orbit with an equator-crossing time of 10:30 A.M. local time. Two identical CERES instruments—Flight Model 1 (FM-1) and 2 (FM-2)—fly alongside MODIS to provide near-global coverage daily. The CERES instrument is a scanning broadband radiometer that measures filtered radiances in the SW (wavelengths between 0.3 and 5 μm), total (TOT) (wavelengths between 0.3 and 200 μm), and infrared window (WN) (wavelengths between 8 and 12 μm) regions. On *Terra*, CERES has a spatial resolution of approximately 20 km (equivalent diameter). One CERES instrument is placed in a cross-track scan mode to optimize spatial sampling for time–space averaging (Young et al. 1998), while the second instrument is either in a rotating azimuth plane (RAP), along-track, or programmable azimuth plane (PAP) scan mode, primarily for the development of ADMs (Loeb et al. 2005), intercalibration with other instruments, and to provide multiangle measurements over specific targets (e.g., field campaigns). The MODIS instrument (Barnes et al. 1998) provides spectral radiance measurements in 36 channels at central wavelengths ranging from 0.41 to 15 μm at three spatial resolutions: 250 m (2 channels), 500 m (5 channels), and 1 km (29 channels). MODIS-viewing geometry is perpendicular to the ground track, with a swath width of 2330 km and scans to a maximum viewing zenith angle (at the ground) of 63°.

In this study, 46 months (March 2000–December 2003) of merged cross-track CERES and MODIS data from the *Terra* edition 2A Single-Scanner Footprint TOA/Surface Fluxes and Clouds (SSF) product are considered. As described in more detail in Loeb et al. (2003, 2005) and Geier et al. (2001), the CERES SSF product combines CERES radiances and fluxes with scene information (e.g., cloud and aerosol properties) from coincident high spatial and spectral resolution MODIS measurements, and meteorological information (e.g., surface wind speed, skin temperature, precipitable water) from the Global Modeling and Assimilation Office (GMAO)'s Goddard Earth Observing System (GEOS) Data Assimilation System (DAS) V4.0.3 product (Suarez et al. 1996). Radiative fluxes are determined using ADMs described in Loeb et al. (2005).

Aerosol properties in the SSF product are determined from the following two sources: (i) by applying the National Oceanic and Atmospheric Administration (NOAA)/National Environmental Satellite, Data, and Information System (NESDIS) algorithm that is described in Ignatov and Stowe (2002) to the MODIS measurements that are determined to be cloud free (Ignatov et al. 2005); and (ii) directly from the MODIS aerosol product (MOD04) (Remer et al. 2005). The NOAA/NESDIS aerosol algorithm is run routinely as part of the CERES data processing at the National Aeronautics and Space Administration (NASA) Langley Atmospheric Science Data Center, together with other standard CERES data products. The MOD04 product is processed at the NASA Goddard Space Flight Center (GSFC) Distributed Active Archive Center (DAAC). In the SSF, aerosol retrievals are averaged over CERES footprints by accounting for the CERES point-spread function (Smith 1994) to provide a close spatial match between the CERES radiance measurements and the aerosol information.

The NOAA/NESDIS SSF aerosol parameters (hereafter referred to as NOAA SSFconsidered here include the 0.63-μm aerosol optical depth and the corresponding average MODIS radiances at 0.644 (channel 1) and 1.632 (channel 6) μm. To compare NOAA SSF aerosol optical depths with MOD04 retrievals at 0.644 μm, the NOAA SSF 0.63-μm aerosol optical depths are scaled by a factor of 0.96377 (Ignatov et al. 2005). Because of space limitations, the SSF product retains only a subset of MOD04 parameters. Over ocean, MOD04 aerosol optical depths at seven wavelengths are recorded in the SSF, but the associated radiances are not saved. Consequently, MOD04 radiances are obtained directly from the original MOD04 files that are provided by the GSFC DAAC. To clearly distinguish between results that are determined using MOD04 parameters in the SSF product from those in the original MOD04 product, we refer to the former as "MOD04 SSF" and the latter as simply "MOD04."

Two cloud masks are used in the SSF product to provide two sets of clear-sky MODIS radiances. The CERES cloud mask (Minnis et al. 2003) uses data in five channels to determine whether individual pixels contain cloud, glint, smoke, or fire signatures. The CERES cloud mask uses a series of threshold tests to compare the pixel value to a known background clear-sky value for reflectance, brightness temperature, and infrared/near-infrared difference. The threshold values for these tests are determined from several sources, including empirically derived clear-sky albedo maps, surface skin temperature from numerical weather analyses, atmospheric temperature and humidity profiles (also from numerical weather analyses), and empirical spectral surface emissivity maps (Trepte et al. 1999). Pixels that are identified as being cloudy are further analyzed to determine cloud properties, such as cloud phase, optical depth, cloud-top temperature, and particle effective radius (Minnis et al. 2003). The SSF product retains the cloud properties, the fraction of MODIS pixels that are identified as clear in a CERES footprint (according to the CERES cloud mask), and the average MODIS radiances in five channels corresponding to the clear and cloudy areas.

The NOAA SSF cloud mask considers only pixels with a glint angle $>40°$ on the antisolar side of the MODIS swath. Pixels that are identified as being clear by the CERES cloud mask are subjected to two additional threshold tests. The first is a spatial homogeneity test that is applied to MODIS pixels: if the maximum and minimum 0.644-μm reflectances from a 2×2 subsampled MODIS pixel array differ by more than a threshold value of 0.003, the pixels are considered to be potentially cloud contaminated. "Subsampled" here means that only every forth MODIS pixel from every second scan line is considered. The second test is an adjacency test that requires all pixels surrounding a candidate pixel to be clear. If a pixel passes these two tests, the NOAA/NESDIS aerosol retrieval algorithm (Ignatov and Stowe 2002) is applied to determine aerosol optical depth. Additionally, in order to minimize misclassification of heavy aerosols as clouds, pixels that are identified as being cloudy by the CERES cloud mask are further tested: if the pixel's 3.7-μm reflectance is less than 0.03, the pixel is assumed to be clear and a retrieval is performed. Thresholds for these tests are selected based on the analysis of Stowe et al. (1999).

The MOD04 product uses cloud screening and aerosol retrieval algorithms that are developed by the MODIS cloud and aerosol groups (Tanré et al. 1996; Ackerman et al. 1998; Martins et al. 2002; Remer et al. 2005). Only pixels with a glint angle $>40°$ are considered. The cloud screen algorithm (Martins et al. 2002; Remer et al. 2005) relies primarily on the spatial variability in visible reflectances over three-by-three 500-m pixel arrays to separate aerosol from cloud. If the standard deviation in reflectance at 0.55 μm from the 3×3 pixel array is greater than 0.0025, all nine pixels in the group are labeled as being cloudy and are discarded (Martins et al. (2002). Heavy dust aerosols that fail the spatial variability test are identified using the ratio of reflectances at 0.47 and 0.644 μm (dust absorbs radiation at blue wavelengths, while clouds are spectrally flat). Thick, spatially uniform clouds are avoided by rejecting pixels whose reflectance at 0.47 μm exceed a threshold of 0.40. Cirrus clouds are screened using a combination of infrared and near-infrared tests that are provided by the standard MODIS cloud mask (Ackerman et al. 1998; Gao et al. 2002). A sediment mask is also used to identify ocean scenes that are contaminated by river sediments (Li et al. 2003).

3. Clear-sky SW direct radiative effect of aerosols

The clear-sky SW DREA is defined as the difference between SW radiative fluxes in the absence and presence of aerosol in cloud-free conditions. In Loeb and Kato (2002), the DREA was determined from clear-sky CERES TRMM footprints using empirical ADMs to convert the SW radiance measurements to radiative fluxes. The contribution from clear regions at spatial scales that are smaller than a CERES TRMM footprint ($\sim$10 km equivalent diameter at nadir) was, therefore, missing from that analysis. Because the *Terra* orbit altitude (705 km) is approximately twice that of TRMM (350 km), the nominal spatial resolution of CERES *Terra* is reduced by a factor of 4 ($\sim$20 km equivalent diameter at nadir) compared to CERES TRMM. By restricting the analysis of the DREA to include only clear-sky CERES *Terra* footprints, the aerosol sampling problem is exacerbated even further: regions whose meteorology favors large-scale clear-sky conditions are oversampled, while smaller-scale clear-sky regions (e.g., clear breaks in broken cloud conditions) are undersampled.

To overcome this problem, the approach of Loeb and Kato (2002) is generalized in order to account for the radiative effect of aerosols at sub-CERES spatial scales. Instead of limiting the analysis to clear-sky CERES footprints, we now determine TOA fluxes directly from higher-resolution MODIS measurements that are determined to be clear, regardless of whether cloud is present in a CERES footprint. The clear-sky MODIS radiances that are considered are the same as those that are used to determine aerosol retrievals in either the NOAA SSF or MOD04 products. The radiances are converted to broadband SW radiances by applying a narrow-to-broadband conversion, and TOA fluxes are estimated using the CERES ADMs (Loeb et al. 2003). To convert MODIS narrowband radiance measurements to a broadband SW radiance estimate ($\hat{I}_{\rm SW}$), the following expression is used:

$$\hat{I}_{\rm SW} = a_0 + \sum_{i=1}^{N_\lambda} a_i I_i, \tag{1}$$

where a_is are regression coefficients, and I_is correspond to narrowband MODIS radiances in N_λ channels. The regression coefficients are determined monthly by relating clear-sky CERES SW radiances with coincident MODIS narrowband radiances for discrete intervals of the solar zenith angle (10° increments), viewing zenith angle (10° increments), and relative azimuth angle (20° increments). To convert NOAA SSF clear-sky MODIS radiances to SW radiances, we develop a two-channel narrow-to-broadband regression relation between clear-sky CERES SW radiances and MODIS radiances at 0.644 (channel 1) and 1.632 (channel 6) μm. To convert MOD04 clear-sky radiances to SW radiances, a three-channel narrow-to-broadband regression is developed between clear-sky CERES SW radiances and MODIS radiances at 0.644, 0.858, (channel 2), and 1.632 μm. The NOAA SSF narrow-to-broadband regression uses only two MODIS channels because aerosol retrievals from the NOAA SSF algorithm are only available in two channels.

To evaluate the error in the regression algorithm, predicted broadband radiances from MODIS are compared with CERES measurements. Figures 1 and 2 show histograms of the bias and regional root-mean-square (rms) error determined from clear-sky CERES footprints in 1° latitude × 1° longitude regions within larger latitude–longitude zones for June–July–August (JJA) 2000, and December 2000–January 2001–February 2001 (DJF), respectively. Table 1 summarizes the average bias and rms errors in each latitude–longitude zone. Globally, the average relative bias error resulting from the narrow-to-broadband conversion is approximately −0.5%, and the relative rms error is approximately 2.75%. In terms of a 24-h-averaged SW flux uncertainty, this corresponds to a bias of −0.2 W m^{-2} and an rms error of 1 W m^{-2}. Regionally, relative bias errors remain <2%, on average (Table 1), and relative rms errors remain <5%. The largest biases occur over the tropical Pacific Ocean (e.g., 0°–30°N, 90°E–180°).

The monthly mean TOA DREA for a given location at latitude (Θ) and longitude (Φ) is estimated from the following:

$$\Delta F_{\rm SW}^{\rm clr}(\Theta, \Phi) = \frac{1}{N_d}\sum_{d=1}^{N_d}[F_{\rm SW}^{\rm na}(\Theta, \Phi; d) - F_{\rm SW}^{\rm clr}(\Theta, \Phi; d)], \tag{2}$$

where $F_{\rm SW}^{\rm na}(\Theta, \Phi; d)$ is the daily average SW flux in the absence of aerosols, $F_{\rm SW}^{\rm clr}(\Theta, \Phi; d)$ is the daily average SW flux in the presence of aerosols, and N_d is the number of days (d) in the month; $F_{\rm SW}^{\rm clr}(\Theta, \Phi; d)$ is determined from all clear-sky SW radiances ($\hat{I}_{\rm SW}$) falling in (Θ, Φ) on day d. Each $\hat{I}_{\rm SW}$ value is first converted to an instantaneous TOA flux by correcting for the anisotropy of the scene using empirical ADMs that are developed from CERES (Loeb et al. 2005). The instanta-

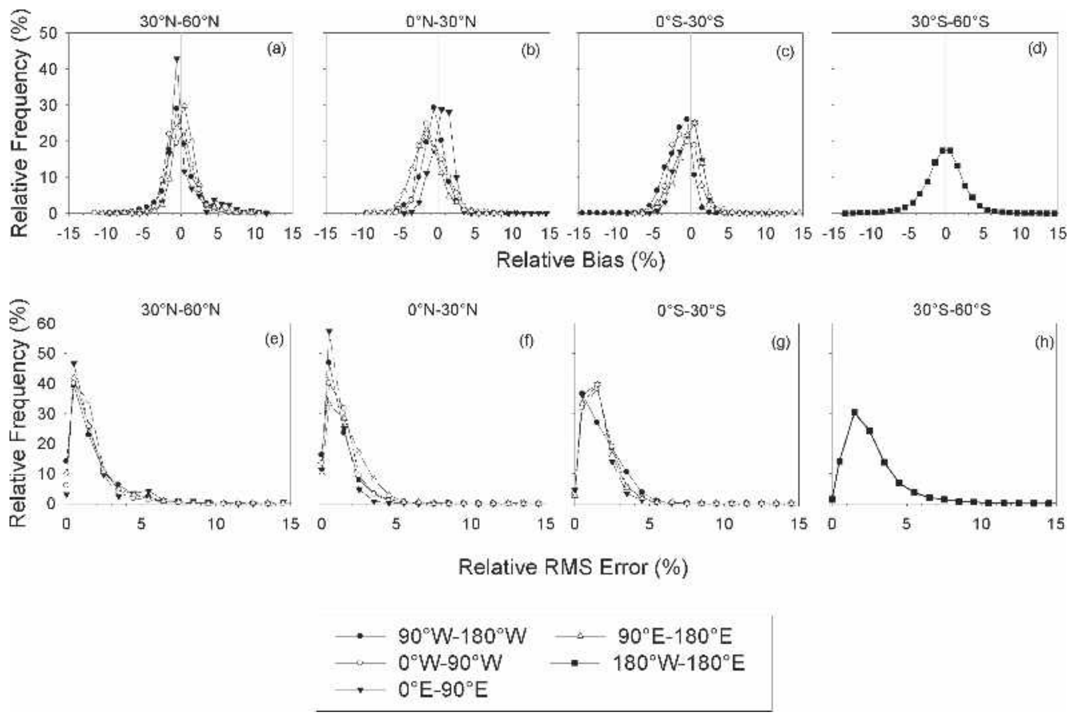

FIG. 1. (a)–(d) Relative bias and (e)–(h) relative rms errors in SW radiance from narrow-to-broadband regression fits for 1° lat × 1° lon regions within the indicated lat–lon zones for JJA (2000).

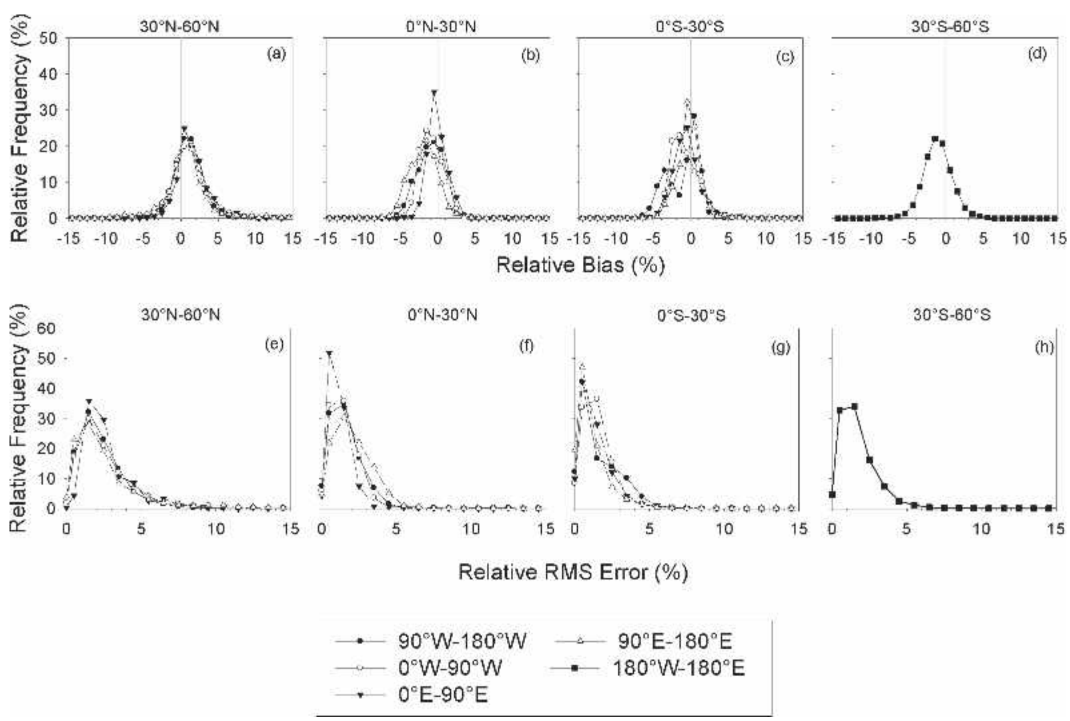

FIG. 2. Same as Fig. 1, but for DJF (2000/01).

Table 1. Relative bias and relative rms errors in SW radiance from narrow-to-broadband regression fits for 1° lat × 1° lon regions within the indicated lat–lon zones for JJA (2000) and DJF (2000/01).

		JJA 2000			DJF 2000/01		
Lat (°)	Lon (°)	Mean radiance ($W\ m^{-2}\ sr^{-1}$)	Relative error (%)	Rms error (%)	Mean radiance ($W\ m^{-2}\ sr^{-1}$)	Relative error (%)	Rms error (%)
30°–60°N	90°W–180°	18.8	−0.2	2.8	12.4	1.1	3.6
30°–60°N	0°–90°W	19.2	−0.2	2.8	12.1	1.1	4.2
30°–60°N	0°–90°E	21.5	0.5	3.7	12.3	1.8	4.6
30°–60°N	90°E–180°	20.0	0.5	2.9	14.2	0.8	4.6
0°–30°N	90°W–180°	20.2	−0.6	2.3	17.8	−1.0	2.8
0°–30°N	0°–90°W	22.4	−0.6	2.9	18.5	−0.9	3.0
0°–30°N	0°–90°E	23.5	0.5	2.1	20.5	−0.1	2.4
0°–30°N	90°E–180°	19.7	−1.5	2.7	18.5	−1.9	3.3
0°–30°S	90°W–180°	15.6	−1.7	3.0	21.5	−1.1	2.8
0°–30°S	0°–90°W	15.5	−0.9	2.7	21.8	−0.9	2.6
0°–30°S	0°–90°E	15.7	−0.3	2.6	21.9	−0.6	2.6
0°–30°S	90°E–180°	15.9	−0.4	3.1	21.8	−0.3	2.4
30°–60°S	180°–180°	9.7	−0.2	4.1	19.3	−1.1	3.0

neous TOA flux is then converted to a 24-h mean TOA flux by applying diurnal albedo models to estimate what the reflected SW flux would be at all local times of the day, assuming there are no changes in aerosol or surface properties, and averaging these fluxes over the full 24 h of local time. Mathematically, this procedure is as follows:

$$\hat{F}_{24h} = \frac{\hat{A}[\theta_o(t_o)]}{\alpha_j[\theta_o(t_o)]}\left\{\frac{1}{N_t}\sum_{i=1}^{N_t}\alpha_j[\theta_o(t_i)]\mu_o(t_i)E_o\right\}, \quad (3)$$

where $\hat{A}$ is the estimated instantaneous TOA albedo that is inferred by dividing the instantaneous TOA flux by the incident solar irradiance $\mu_o(t_o)E_o$, where μ_o and E_o are the cosine of the solar zenith angle (θ_o) and the incident solar irradiance at the TOA, respectively, and t_o is time of observation; α_j is the scene-dependent diurnal albedo model, N_t is the number of time steps used to determine the 24-h-averaged flux, and t_i is the local time corresponding to the ith time step. The α_js were determined from ADMs that were developed using CERES TRMM measurements for 561 scene types, defined as a function of wind speed (clear ocean), cloud fraction, cloud phase, cloud optical depth, and surface type (Loeb et al. 2003). The reason that diurnal albedo models from TRMM are used is because the TRMM spacecraft is in a precessing orbit with a 46-day repeat cycle, which means that the full range of solar zenith angles that are needed to develop the diurnal albedo models is acquired over a region every 46 days. In practice, to apply Eq. (3) on a footprint-by-footprint basis, the summation $(1/N_t)\Sigma_{i=1}^{N_t}\alpha_j[\theta_o(t_i)]\mu_o(t_i)E_o$ is precalculated and stored as a lookup table as a function of Julian day, scene type, and latitude. The calculations are performed with temporal resolution of 1 min and stored at every 1° latitude increment.

The daily average flux in the absence of aerosols $F_{SW}^{na}(\Theta, \Phi; d)$ is inferred from the relationship between SW TOA flux and aerosol optical depth. In each 1° interval of solar zenith angle where data are available, instantaneous TOA fluxes are plotted against aerosol optical depth, and a regression line is fit to the data. The intercept of these regressions—that is, the TOA flux that is extrapolated to zero aerosol optical depth—approximates the mean "no aerosol flux" as a function of solar zenith angle. The 24-h mean flux $F_{SW}^{na}(\Theta, \Phi; d)$ is determined following the procedure that is described in Eq. (3) using the CERES TRMM diurnal albedo models. Kato et al. (2002) examined the uncertainty in this approach by comparing empirically based "no aerosol" fluxes from seventy-two 20° latitude × 20° longitude regions and concluded that F_{SW}^{na} can be determined to within 1 W m^{-2} in any given region. The main sources of error are uncertainties in CERES-derived fluxes, aerosol optical depth retrievals, and variations in surface wind speed.

a. Seasonal comparisons

With the approach outlined above, the DREA at spatial scales as small as individual MODIS pixels are accounted for, thereby avoiding the sampling bias that occurs when only cloud-free CERES footprints are considered. However, in the vicinity of clouds, the separation between clear and cloudy pixels is often difficult to discern, even with high spatial and temporal resolution measurements, because the transition between clear and cloudy areas is not always sharp, but often occurs gradually in radiometric measurements (Martins

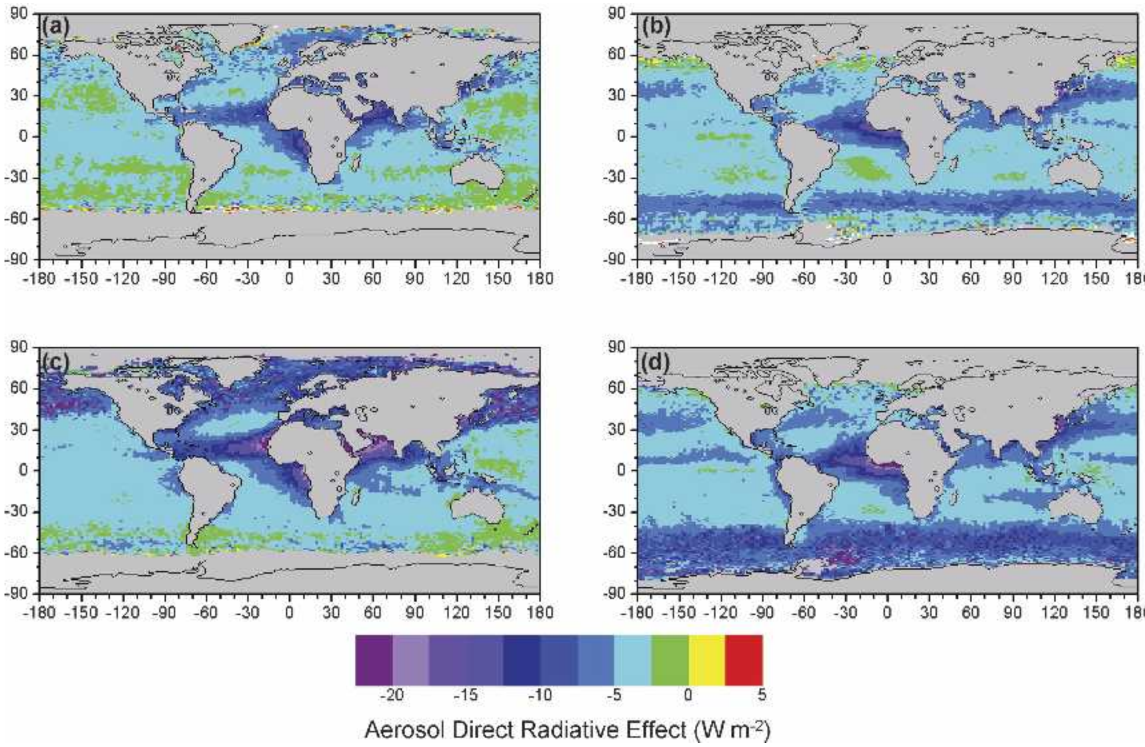

FIG. 3. Direct radiative effect of aerosols based on cloud-free MODIS radiances identified using the NOAA SSF algorithm for (a) JJA (2000) and (b) DJF (2000/01), and the MOD04 algorithm for (c) JJA (2000) and (d) DJF (2000/01).

et al. 2002; Liu et al. 2004). At high relative humidities, the uptake of water vapor by unactivated aerosol, combined with large spatial gradients in relative humidity, likely makes it difficult to distinguish between aerosol and cloud using conventional spectral techniques (R. J. Charlson 2004, personal communication). Furthermore, in areas of heavy aerosol (e.g., dust, smoke, pollution), it is often difficult to distinguish between aerosol and cloud from passive remote sensing methods (Geogdzhayev et al. 2004).

To investigate the influence of different cloud masks on the DREA, Figs. 3a–d show the DREA that is determined using cloud-free MODIS pixels identified with the NOAA SSF and MOD04 algorithms for JJA (2000) and DJF (2000/01). The corresponding aerosol optical depths at 0.644 μm are provided in Figs. 4a–d. The DREA from both algorithms shows a marked increase as a result of dust off of the Sahara and Saudi Arabian deserts, as well as from the deserts of Mongolia and China. In some coastal regions, the SW radiative cooling by dust exceeds 20 W m^{-2}. In JJA, the Asian dust extends across to the Pacific Ocean, and the DREA that is inferred from MOD04 radiances reaches 30 W m^{-2} as far east as 150°W. Near 60°S, there is also a significant DREA in DJF, an area that also exhibits substantial cloud radiative forcing (Harrison et al. 1990). If this is aerosol, it is likely sea salt aerosol, associated with high wind speeds that are common at those latitudes. It is also quite possible that some of this is cloud contamination by low-level broken clouds that is mistakenly identified as aerosol. Far from major aerosol sources, 0.644-μm aerosol optical depths are generally <0.2, and reach 1.0 close to desert regions.

Regional differences between NOAA SSF and MOD04 DREA and aerosol optical depth are shown in Figs. 5a–d. In JJA, the two approaches yield similar results far from regions that are influenced by desert dust. Near the Sahara and Saudi Arabian deserts, the DREA (aerosol optical depth) from MOD04 is larger by up to 10 (0.3) W m^{-2}, compared to NOAA SSF. Differences are even larger in the northeastern Pacific Ocean regions that are influenced by aerosol transported from Asia. In those areas, the DREA (aerosol optical depth) from MOD04 exceeds NOAA SSF by up to 35 (1.0) W m^{-2}. While the regional patterns of differences in the DREA and aerosol optical depth are quite similar to one another in JJA, they differ markedly in DJF. In regions of dust, the DJF differences in the DREA are pronounced, whereas aerosol optical depth differences are small. Between 0° and 30°S, NOAA SSF aerosol optical depths exceed those from MOD04 by up to 0.08, whereas NOAA SSF and

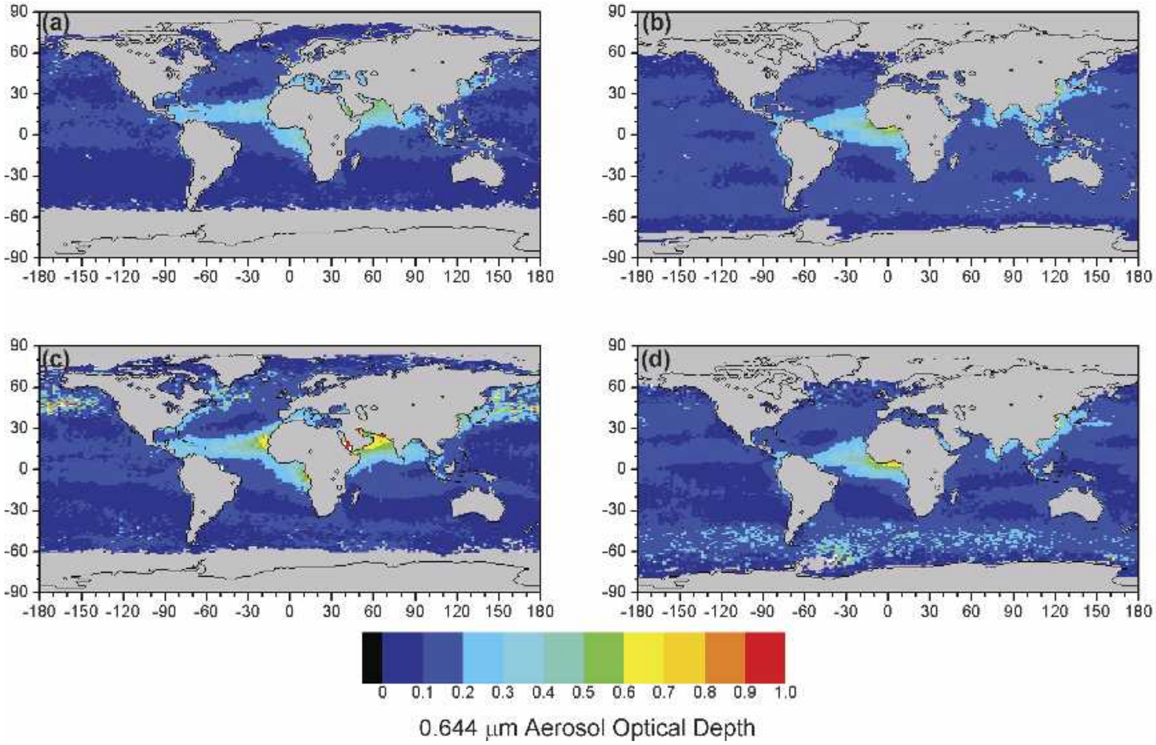

FIG. 4. The 0.644-μm aerosol optical depth from the NOAA SSF algorithm for (a) JJA (2000) and (b) DJF (2000/01), and the MOD04 algorithm for (c) JJA (2000) and (d) DJF (2000/01).

MOD04 estimates of the DREA are similar. These seasonal differences in aerosol optical depth are likely the result of the different assumptions about aerosol microphysical properties in the NOAA SSF and MOD04 algorithms.

To further investigate sampling differences between MOD04 and NOAA SSF, we perform an analysis similar to that of Ignatov et al. (2005), whereby aerosol optical depth retrievals are stratified according to the cloud fraction over a CERES footprint. Cloud fraction is determined from the CERES cloud mask (Minnis et al. 2003) that is applied to MODIS pixels in a CERES footprint (section 2). Figures 6a–d and Figs. 7a–d show NOAA SSF and MOD04 SSF aerosol optical depth against cloud fraction over CERES footprints for JJA and DJF, respectively, for the following two populations of CERES footprints: (i) all CERES footprints having at least one MODIS pixel aerosol retrieval by either algorithm (Figs. 6a and 7a), and (ii) only those footprints where both NOAA SSF and MOD04 SSF retrievals are available (Figs. 6b and 7b). The latter are referred to as the "intersection" population in Ignatov et al. (2005). Assuming that both algorithms considered the same pixels within a CERES footprint, the intersection results (Figs. 6b and 7b) represent algorithm differences.

MOD04 SSF and NOAA SSF aerosol optical depths both increase with cloud fraction in Figs. 6 and 7. The cause for this relationship may simply be meteorological—cloud cover and aerosol optical depth are both correlated with relative humidity and wind speed. As relative humidity increases, water uptake by aerosols (determined by the solubility of the particle mass) changes the aerosol particle size, density, refractive index, and scattering extinction (e.g., Clarke et al. 2002). This, together with larger wind speeds (which increase sea salt particles), lead to larger aerosol optical depths. Results in Figs. 6 and 7 may also be influenced by cloud contamination in both aerosol products. As noted earlier, cloud masks often use fixed thresholds that are meant to distinguish between clear and cloudy pixels, despite the fact that the transition from clear to cloudy regions is often continuous with no obvious abrupt transition. Cloud mask differences may also explain why the rate of increase in aerosol optical depth with cloud fraction is different for NOAA SSF and MOD04 SSF.

Figures 6c and 7c also show that the largest difference in sampling between MOD04 and NOAA SSF occurs when the cloud fraction exceeds 95%. In this cloud fraction interval, there are approximately 20 times more CERES footprints with aerosol retrievals

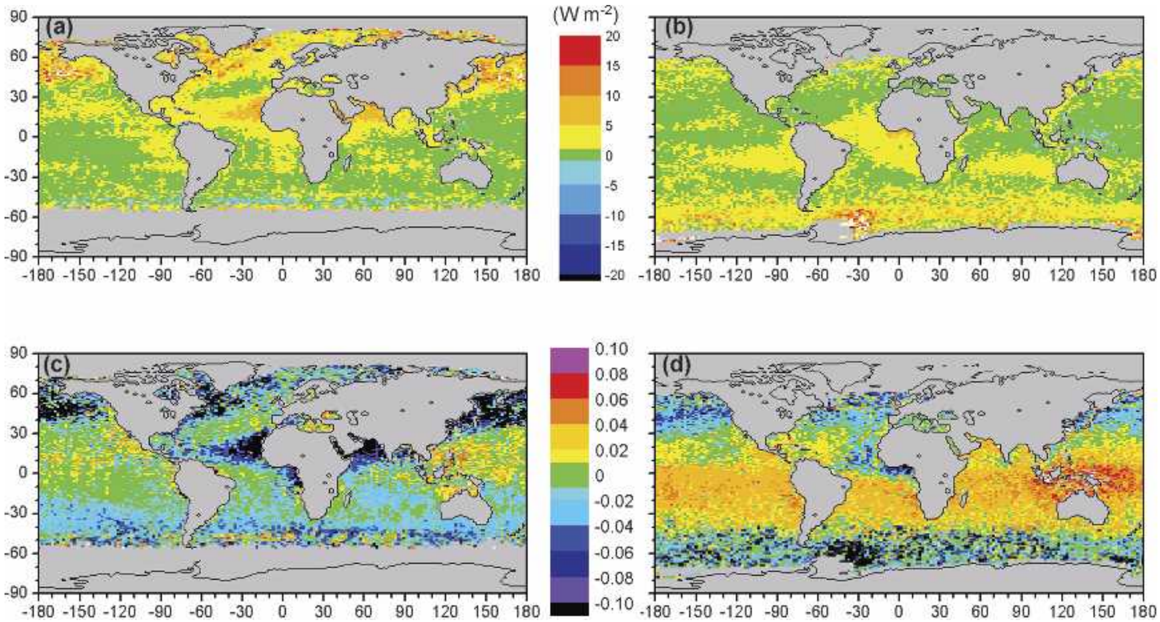

FIG. 5. Difference between aerosol direct effect determined from clear radiances identified using the NOAA SSF algorithm and the MOD04 algorithm (NOAA SSF minus MOD04) for (a) JJA (2000) and (b) DJF (2000/01); difference in 0.644-μm aerosol optical depth between NOAA SSF and MOD04 approaches for (c) JJA (2000) and (d) DJF (2000/01).

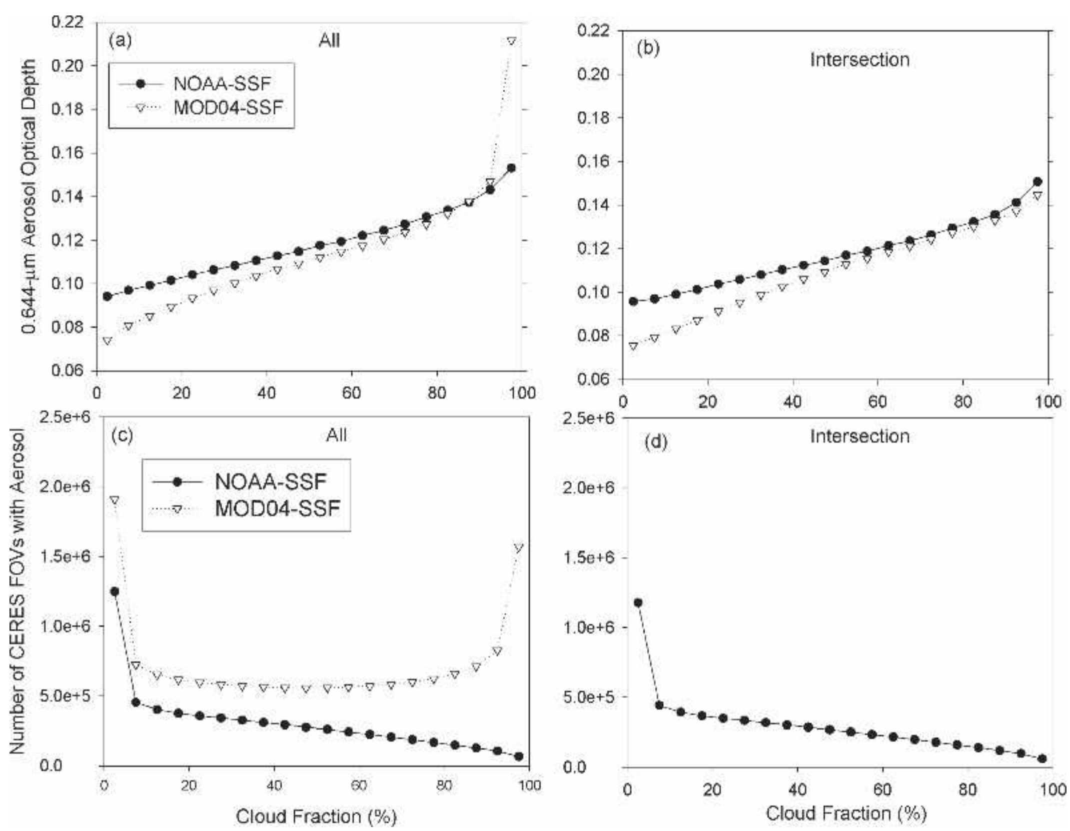

FIG. 6. JJA (2000) 0.644-mm aerosol optical depth against cloud fraction for (a) all CERES footprints with aerosol retrievals ("all") and (b) only CERES footprints with both NOAA SSF and MOD04 aerosol optical depth retrievals ("intersection"); (c) and (d) the corresponding number of CERES footprints considered.

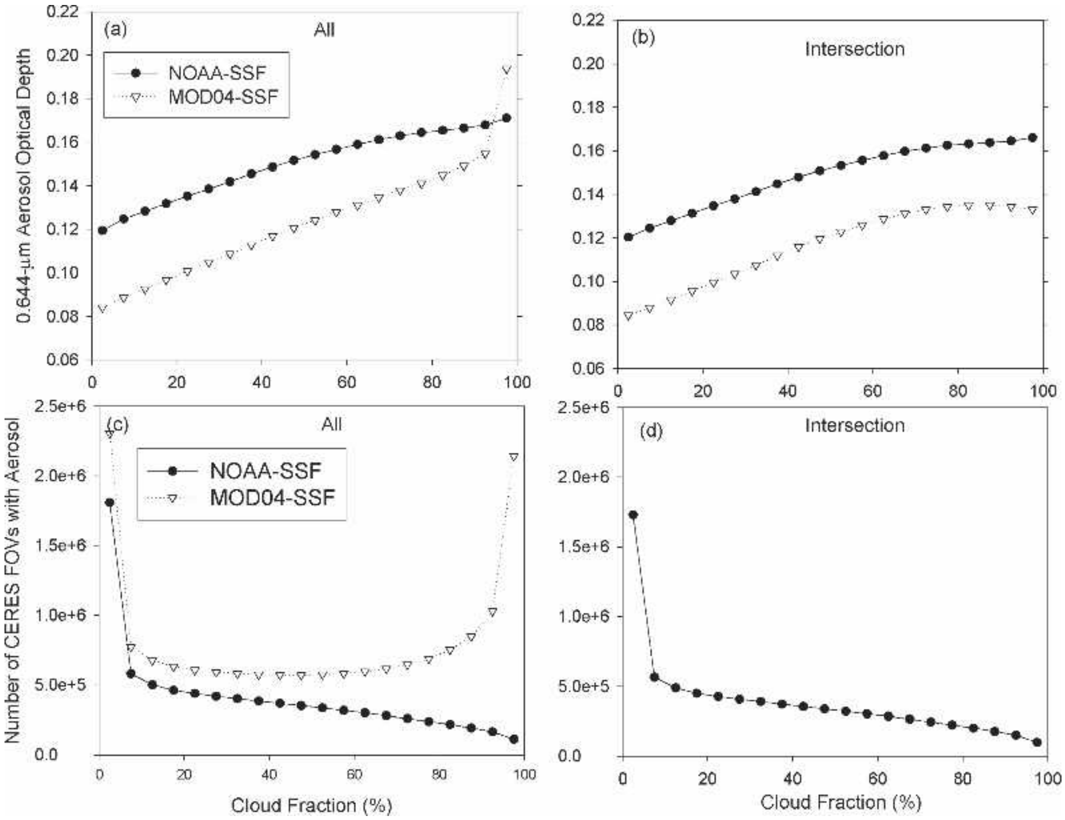

FIG. 7. Same as Fig. 6, but for DJF (2000/01).

from MOD04 as there are from NOAA SSF. MOD04 aerosol optical depths exceed NOAA SSF values by 0.059 (32%) in JJA, and by 0.023 (12%) in DJF (Fig. 6a and 7a). The reason for the large increase in the MOD04 sampling for cloud fraction >95% is the result of a misclassification of either cloud as dust aerosol by MOD04 or dust as cloud by the CERES cloud mask. Figure 8 shows the regional distribution of footprints that are identified as being overcast by CERES that also contain MOD04 aerosol retrievals. Most regions where discrepancies occur are in areas that are influenced by dust aerosol (e.g., off the coasts of the Sahara and Saudi Arabian deserts). Clearly, more study is needed to verify why such large sampling differences occur. Visual inspection of individual scenes can help resolve some of these discrepancies, but that approach is limited because it is labor intensive and highly subjective. Alternately, it may also be useful to compare the satellite-derived frequency of occurrence of clear scenes with surface observations, but that is limited to only a small portion of the earth. Perhaps the best validation will come when global measurements from the Cloud-Aerosol Lidar and Infrared Pathfinder Satellite Observation (CALIPSO) (Winker et al. 2003) will be available. CALIPSO will provide high-resolution vertical profiles of lidar backscatter that will enable better discrimination between dust and cloud.

Global seasonal and annual average DREA and 0.644-μm aerosol optical depth are provided in Table 2 for March 2000 through February 2001. In all seasons, radiative cooling by aerosols inferred from MOD04 clear-sky radiances is 1–2 W m^{-2} (35%–55%) larger than that obtained from NOAA SSF. Radiative cooling is strongest in March–May (MAM), reaching 6 W m^{-2} from MOD04, and 4.3 W m^{-2} from NOAA SSF. Because the same approach is used to determine the DREA in both cases, differences between MOD04 and NOAA SSF are due only to differences in cloud screening. In contrast, NOAA SSF and MOD04 aerosol optical depth differences are the result of both cloud mask and algorithm (two-channel versus single-channel retrievals) differences (Ignatov et al. 2005). Forcing efficiencies that are derived from the ratio of the global average DREA and 0.644-μm aerosol optical depth are -32 and -41 W m^{-2} τ^{-1} for NOAA SSF and MOD04, respectively. In other studies, satellite-derived TOA forcing efficiency over ocean with respect to aerosol optical depth at 0.55 μm ranges from -35 to -52 W m^{-2} τ^{-1}, with an average value of approximately -40 W m^{-2} τ^{-1} (Anderson et al. 2004, manuscript submit-

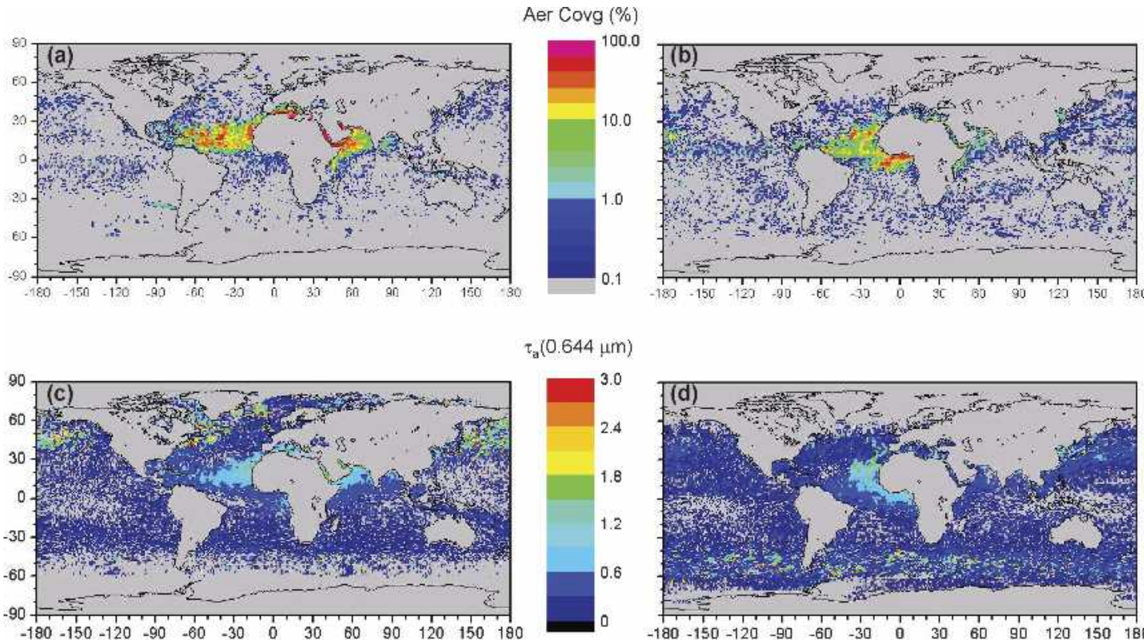

FIG. 8. MOD04 aerosol coverage in CERES footprints identified as overcast by the CERES cloud mask for (a) JJA and (b) DJF, and corresponding mean MOD04 0.644-μm aerosol optical depth for (c) JJA and (d) DJF.

ted to *Bull. Amer. Meteor. Soc.*). The corresponding MOD04 forcing efficiency with respect to the 0.55-μm aerosol optical depth is -38 W m^{-2} τ^{-1}, while it is -29 W m^{-2} τ^{-1} for NOAA SSF.

Figures 9a and 9b compare hemispheric averages of the DREA from NOAA SSF, MOD04, and Table 1 of Chou et al. (2002). Chou et al. (2002) estimated the DREA from SeaWiFS-retrieved aerosol optical properties for January–December 1998, and provide global, Northern Hemisphere (NH) and Southern Hemisphere (SH) values for January, April, July, October, and the annual average. In all months, radiative cooling by aerosols is more pronounced in Chou et al. (2002) compared to NOAA SSF. Differences are generally 1–2 W m^{-2}, but reach 2.9 W m^{-2} in the SH during January. The Chou et al. (2002) values of DREA are much closer to those derived from MOD04. The global annual average difference between the two is only 0.06 W m^{-2} (1%), largely because of compensation between the SH and NH differences; SW radiative cooling from Chou et al. (2002) exceeds MOD04 by 0.5 W m^{-2} (11%) in the SH, but is smaller than MOD04 in the NH by 0.65 W m^{-2} (11%). The largest difference between Chou et al. (2002) and MOD04 occurs in the NH during April and July, where the MOD04 DREA is larger by up to 2 W m^{-2} (28%). The sign of the difference is reversed in January, and radiative cooling by Chou et al. (2002) is larger by 0.9 W m^{-2} (20%). In the SH, the DREA differences remain <1 W m^{-2}.

TABLE 2. Global average DREA and 0.644-μm aerosol optical depth (AOD) for MAM 2000, JJA 2000, SON 2000, DJF 2000/01, and Mar 2000–Feb 2001 (ALL), inferred from clear-sky MODIS radiances identified by NOAA SSF and MOD04 algorithms.

	NOAA SSF		MOD04	
Season	DREA (W m^{-2})	0.644-μm AOD	DREA (W m^{-2})	0.644-μm AOD
MAM	−4.32	0.129	−6.11	0.151
JJA	−3.46	0.104	−5.43	0.134
SON	−3.62	0.118	−5.12	0.127
DJF	−3.78	0.122	−5.17	0.121
ALL	−3.80	0.118	−5.46	0.133

NOAA SSF and MOD04 aerosol optical depths in Figs. 9c and 9d show a similar hemispheric mean seasonal cycle as the DREA in Figs. 9a and 9b. Large differences between the NH and SH occur during the NH spring and summer, whereas remarkably little difference is observed in September. Between September and February, radiative cooling is stronger in the SH, but the hemispheric difference is much smaller than during the NH summer.

b. Regional interannual variability

To investigate the temporal variation of the DREA, the world's oceans are divided into subregions as de-

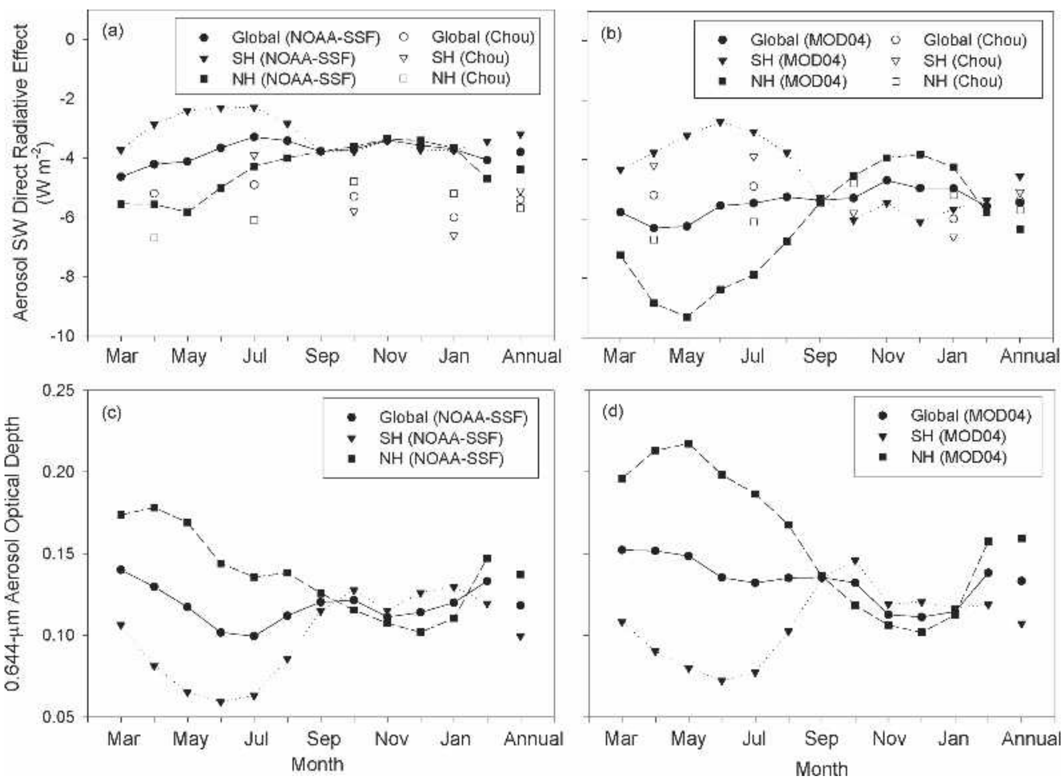

FIG. 9. Comparison of the DREA from (a) NOAA SSF and Chou et al. (2002), and (b) MOD04 and Chou et al. (2002); (c) 0.644-μm aerosol optical depth from NOAA SSF; (d) 0.644-μm aerosol optical depth from MOD04. SH (0°–90°S); NH (0°–90°N).

fined in Fig. 10. Three latitude bands between 30°S and 60°N are split into four regions: 90°W–180°, 0°–90°W, 0°–90°E, and 90°E–180°. A fourth latitude band between 30° and 60°S is also defined without further stratification by longitude. These zones were selected to be consistent with those from the Climate Change Science Program (CCSP) working group on aerosols properties and their impacts on climate (Y. Kaufman 2004, personal communication). The CCSP working group on aerosols will provide a review of measure-

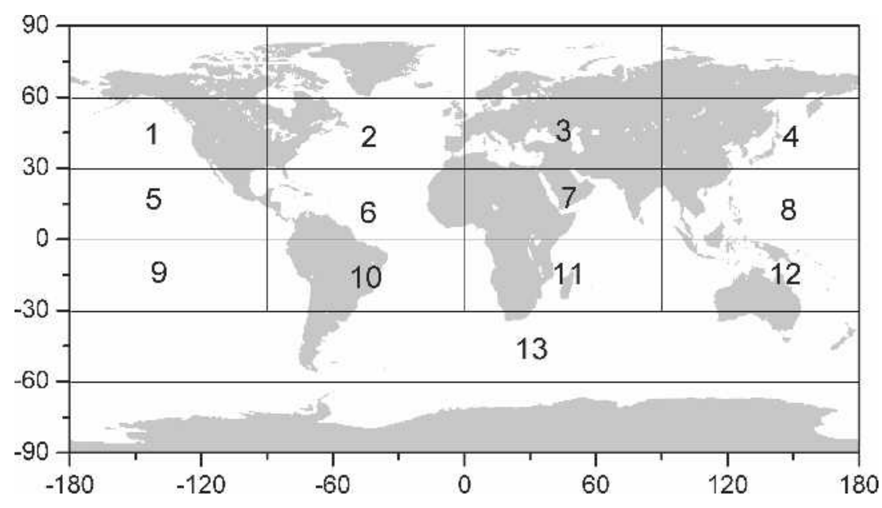

FIG. 10. Regions considered investigating the interannual variability of the aerosol direct radiative effect.

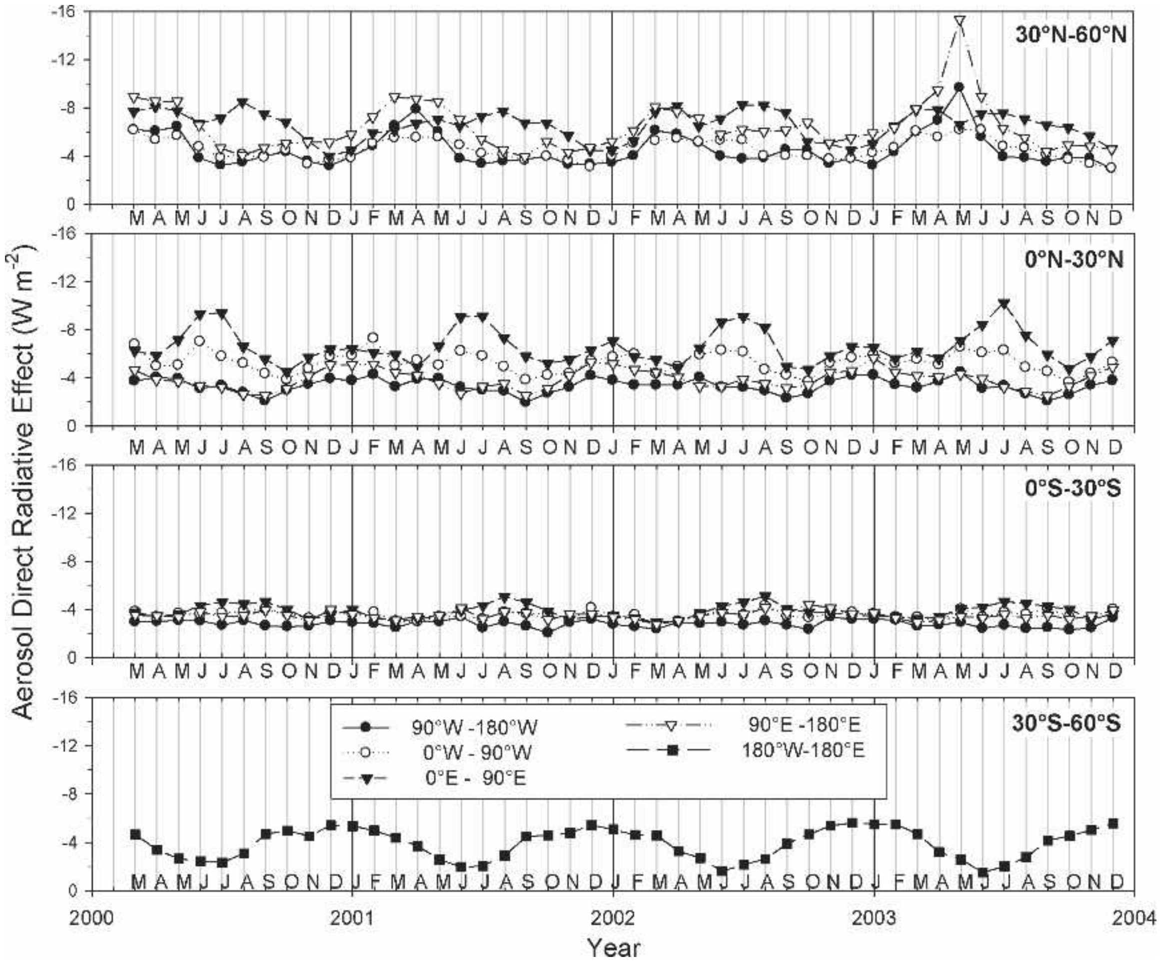

FIG. 11. Regional temporal variations in aerosol direct radiative effect. Clear scenes are identified using NOAA SSF product.

ment-based assessments of the aerosol direct radiative effects (top of atmosphere and at the surface) and the anthropogenic component.

Figures 11–14 provide time series of the regional monthly mean DREA based on the NOAA SSF (Fig. 11), deseasonalized DREA anomaly from 2000 to 2003 (Fig. 12), MOD04 SSF 0.644-μm aerosol optical depth (Fig. 13), and NOAA SSF minus MOD04 SSF 0.644-μm aerosol optical depth difference (Fig. 14). In general, the seasonal variability in the Northern Hemisphere is stronger than in the Southern Hemisphere. A pronounced seasonal cycle in the DREA (Fig. 11) and aerosol optical depth (Fig. 13) is clearly evident over the northern Pacific Ocean between 30° and 60°N (regions 1 and 4 in Fig. 10), with the strongest radiative cooling occurring between March and April. As noted earlier, these regions are influenced by dust aerosol from deserts in northwestern China. The year-to-year variability in the DREA for these regions is striking. In May 2003, the DREA in the northwestern Pacific Ocean (region 4) reaches -15.3 W m^{-2}, which corresponds to a 90% (7.3 W m^{-2}) increase in SW radiative cooling compared to the average May value from the previous 3 yr. The DREA in the northeastern Pacific Ocean (region 1) reaches -9.7 W m^{-2}, corresponding to an increase of 65% (3.8 W m^{-2}) compared to the average May value from prior years. The May 2003 peak is mainly the result of extensive smoke from Siberian forest fires that year. In the region that includes the Mediterranean, Black, and Caspian Seas (region 3), the DREA reaches -8 W m^{-2} in April and August. For 0°–30°N, a highly regular seasonal cycle is observed between 0° and 90°E (region 7). In this region, which includes the Red Sea, Persian Gulf, Arabian Sea, and western Bay of Bengal, DREA reaches approximately -9.5 W m^{-2} in June and July, with a remarkably small year-to-year variation (<1 W m^{-2}) (Fig. 12). The summertime maximum is mainly the result of large-scale aerosol transport from the Arabian Desert to the Arabian Sea during the summer monsoon period (Rajeev

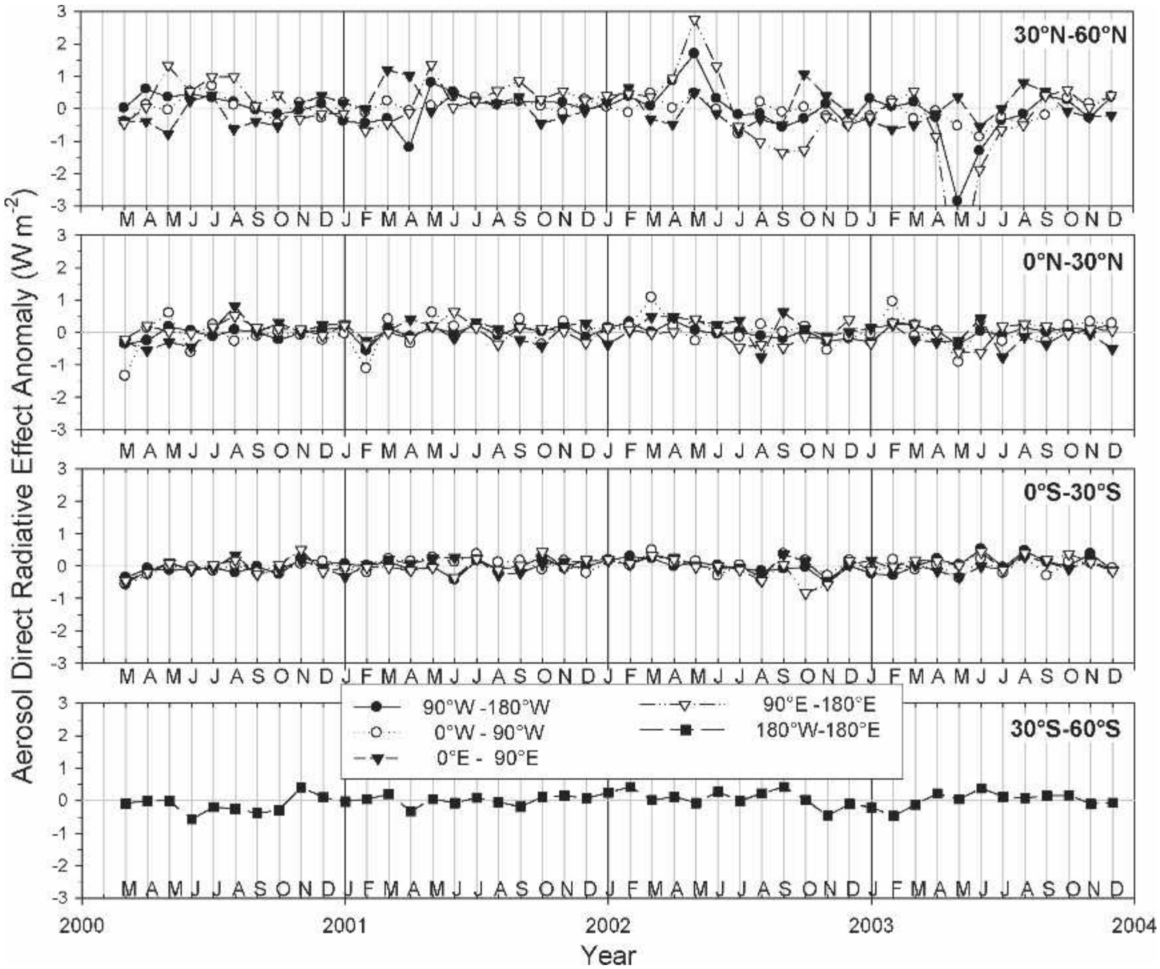

FIG. 12. Same as Fig. 11, but for the deseasonalized aerosol direct radiative effect anomaly from 2000 to 2003.

et al. 2004). Shortwave radiative cooling by aerosols over the southern equatorial ocean for 0°–30°S ranges from 2 to 4 W m^{-2}, with a year-to-year variation in any given month of <0.5 W m^{-2}. Over the southern oceans between 30° and 60°S (region 13), the seasonal cycle is more pronounced, with a minimum SW radiative cooling of approximately 2 W m^{-2} occurring in winter (JJA), and a maximum of approximately 5.5 W m^{-2} in the summer (DJF). MOD04 SSF 0.644-μm aerosol optical depths (Fig. 13) also show a strong seasonal variation, ranging from 0.08 in JJA to 0.16 in DJF. The deseasonalized aerosol direct radiative effect anomaly time series in Fig. 12 shows no systematic trends in any of the regions over the 46-month period.

Differences between NOAA SSF and MOD04 SSF 0.644-μm aerosol optical depths (Fig. 14) are generally largest in the summer months in all regions, except between 30° and 60°S (region 13), where differences are slightly larger in spring (September–October). While the largest differences occur during the same month as the maximum aerosol optical depth for 0°–30°N and 0°–90°E (region 7) (July), the largest aerosol optical depth discrepancies in 30°–60°N over the Pacific Ocean (regions 1 and 4) occur 1 or 2 months after the springtime maximum MOD04 SSF aerosol optical depth. Where there are significant discrepancies between the two algorithms, the NOAA SSF aerosol optical depth is generally smaller than the MOD04 SSF value. The reason for this is undoubtedly associated with differences in cloud screening between the two products, as discussed in section 3a.

4. Total-sky TOA net direct radiative effect of aerosols

Results in the preceding section consider only the SW DREA in cloud-free regions. To provide a more general picture, it is necessary to determine the net DREA (sum of SW and LW DREA) in both clear and cloudy conditions. We estimate the total-sky SW DREA as follows:

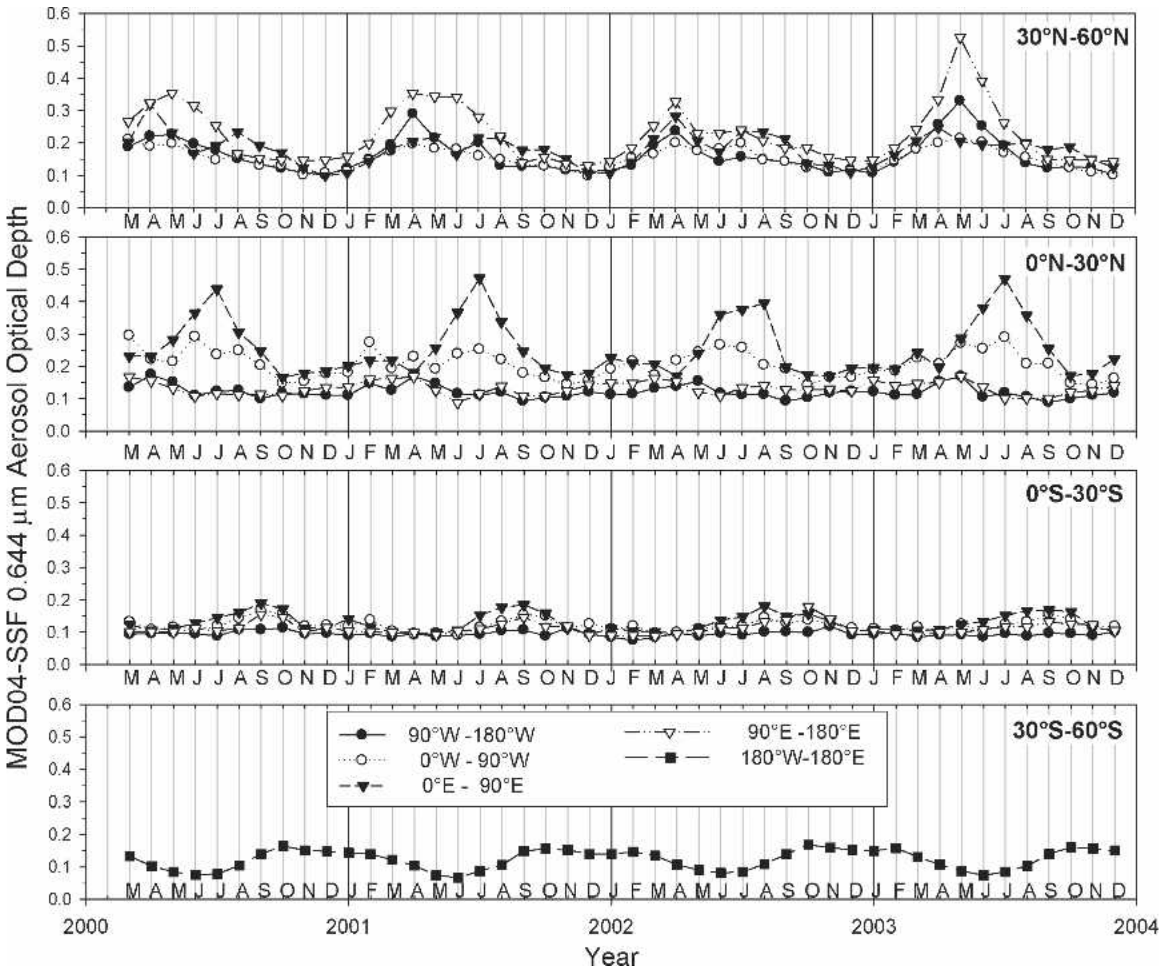

FIG. 13. Same as Fig. 11, but for 0.644-μm aerosol optical depth from MOD04 SSF.

$$\Delta F(\lambda, \phi, d) = \overline{F}_{\mathrm{na}}(\lambda, \phi, d) - \overline{F}_a(\lambda, \phi, d), \tag{4}$$

where $\Delta F_{\mathrm{SW}}^{\mathrm{clr}}$ is the clear-sky SW DREA [Eq. (2)], $\Delta F_{\mathrm{SW}}^{\mathrm{clr}}$ is the DREA in a cloudy column, and $\Delta F(\lambda, \phi, d) = \overline{F}_{\mathrm{na}}(\lambda, \phi, d) - \overline{F}_a(\lambda, \phi, d)$ is the cloud fraction over a CERES footprint, provided for every footprint in the CERES SSF product from either the CERES cloud mask or the MOD04 SSF cloud fraction parameter. Assuming that aerosol scattering in a cloudy column occurs from beneath the cloud layer, an estimate of $\Delta F_{\mathrm{SW}}^{\mathrm{cld}}$ is determined from the following:

$$\Delta F(\lambda, \phi, d) = \overline{F}_{\mathrm{na}}(\lambda, \phi, d) - \overline{F}_a(\lambda, \phi, d), \tag{5}$$

where $\Delta F(\lambda, \phi, d) = \overline{F}_{\mathrm{na}}(\lambda, \phi, d) - \overline{F}_a(\lambda, \phi, d)$ is the transmission through the cloud layer. Substituting Eq. (5) into Eq. (4) yields

$$\Delta F(\lambda, \phi, d) = \overline{F}_{\mathrm{na}}(\lambda, \phi, d) - \overline{F}_a(\lambda, \phi, d), \tag{6}$$

where $\Delta F(\lambda, \phi, d) = \overline{F}_{\mathrm{na}}(\lambda, \phi, d) - \overline{F}_a(\lambda, \phi, d)$ is related to the albedo [$\Delta F(\lambda, \phi, d) = \overline{F}_{\mathrm{na}}(\lambda, \phi, d) - \overline{F}_a(\lambda, \phi, d)$] and absorption [$\Delta F(\lambda, \phi, d) = \overline{F}_{\mathrm{na}}(\lambda, \phi, d) - \overline{F}_a(\lambda, \phi, d)$] over the cloudy portion of the CERES footprint as follows:

$$Tr_{\mathrm{cld}} = 1 - \alpha^{\mathrm{cld}} - a^{\mathrm{cld}}; \tag{7}$$

α^{dd} is estimated from the albedo for the footprint (α^{fov}) and clear area (α^{clr}) as follows:

$$\alpha^{\mathrm{cld}} = \frac{\alpha^{\mathrm{fov}} - (1 - f)\alpha^{\mathrm{clr}}}{f}, \tag{8}$$

where α^{fov} and α^{clr} are inferred from CERES ADMs (Loeb et al. 2005). Based on a sensitivity analysis of radiative transfer model calculations for a range of cloud conditions, we assume a value of 0.2 for α^{clr}. This value also corresponds to the global average according to Kiehl and Trenberth (1997). Note that this approach ignores aerosol above the cloud layer. In polluted regions, this approximation leads to an overestimation of

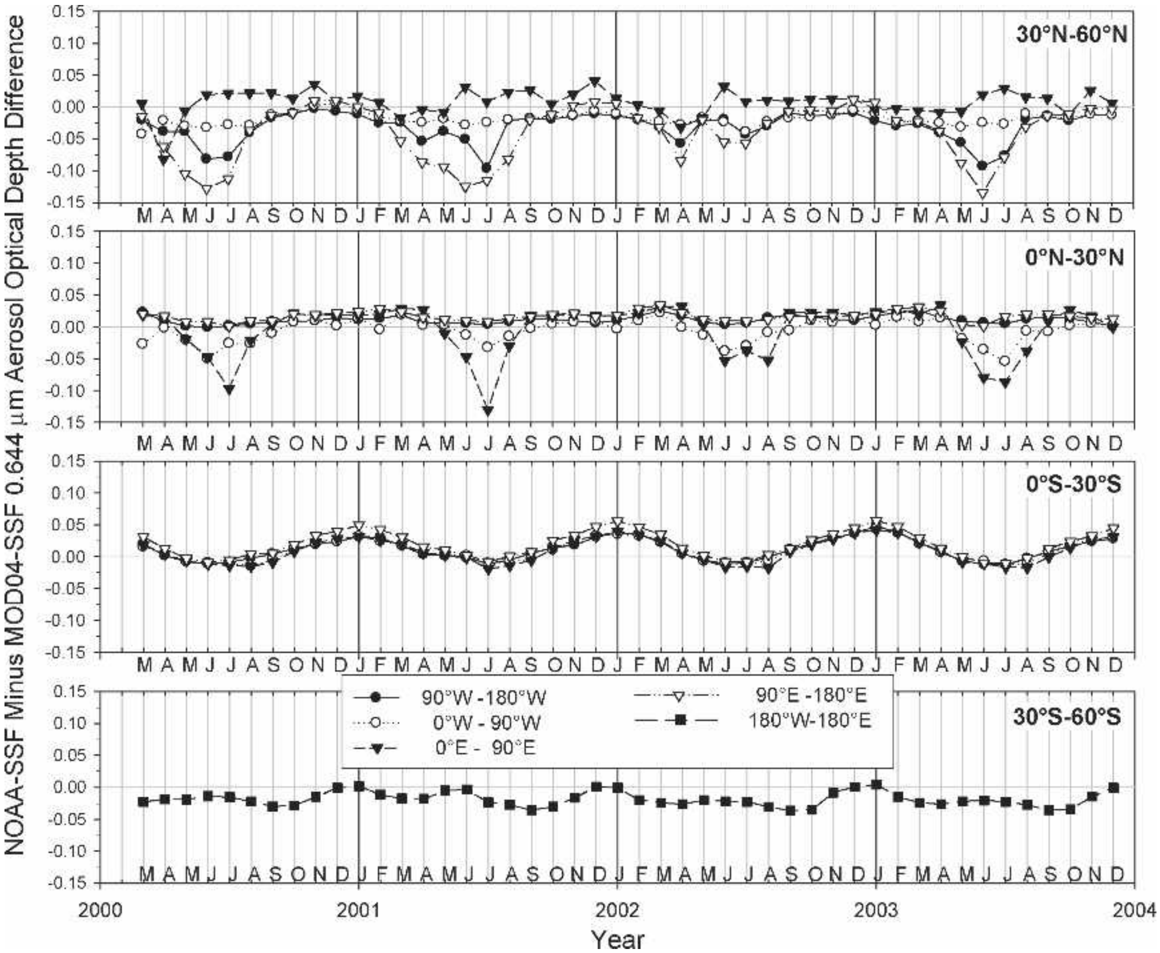

FIG. 14. Same as Fig. 11, but for NOAA SSF minus MOD04 SSF 0.644-μm aerosol optical depth difference.

the radiative cooling effect of aerosols (Ackerman et al. 2000).

An attempt is made to estimate the clear-sky LW DREA empirically by relating the CERES LW flux with MOD04 SSF aerosol optical depth for each of the regions in Fig. 10. A similar approach is used by Zhang and Christopher (2003) over the Sahara Desert for clear-sky conditions. That study relates CERES LW fluxes with aerosol optical depths from the Multiangle Imaging Spectroradiometer (MISR), and finds that dust aerosols have a warming effect over the Sahara Desert with a LW forcing efficiency of 15 W m^{-2} τ^{-1}. In another study, Satheesh and Lubin (2003) estimate the LW radiative forcing efficiency of marine aerosol over the Indian Ocean to range from 4 to 6 W m^{-2} τ^{-1}. Figures 15a and 15b show clear-sky LW flux against 0.644-μm MOD04 SSF aerosol optical depth for region 7 (0°–30°N, 0°–90°E) in JJA and DJF, respectively. CERES footprints are divided into four intervals of sea surface temperature (T_s) corresponding to the 25th, 50th, and 75th percentiles in each season, and LW fluxes are averaged in aerosol optical depth intervals of a 0.02 width. In all cases, LW flux decreases with increasing MOD04 SSF aerosol optical depth, suggesting that the LW radiative effect of aerosols in this region is to warm the clear column. However, the magnitude of the warming is highly variable, ranging from 1 to 16 W m^{-2}. In other regions, where aerosol optical depths remain <1, no clear relationship between LW flux and aerosol optical depth is observed (not shown). To improve this relationship, simultaneous measurements of aerosol height, optical depth, and LW flux are needed. This combination will become available when the CALIPSO lidar flies in formation with CERES and MODIS on the *Aqua* satellite.

Lacking a sound empirical relationship between LW flux and aerosol optical depth for all of the regions in Fig. 10, we approximate the clear-sky LW DREA by assuming a forcing efficiency of 15 W m^{-2} τ^{-1} in regions 6 and 7, where dust aerosol is present in large

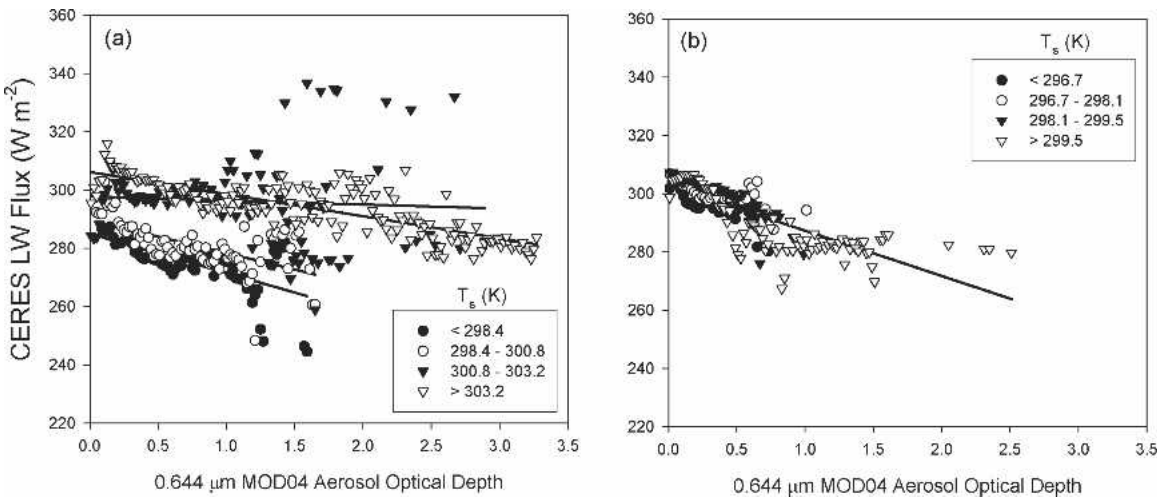

FIG. 15. Clear-sky LW flux against 0.644-μm MOD04 SSF aerosol optical depth and sea surface temperature (T_s) for 0°–30°N and 0°–90°E (region 7) in (a) JJA and (b) DJF.

quantities, and there is a LW forcing efficiency of 5 W m^{-2} τ^{-1} elsewhere, based on results of Satheesh and Lubin (2003). Because the LW effect of aerosols in a cloudy column is expected to be small, it is not considered. The net direct radiative effect of aerosol is, therefore, determined from

$$\Delta F(\lambda, \phi, d) = \overline{F}_{\mathrm{na}}(\lambda, \phi, d) - \overline{F}_a(\lambda, \phi, d), \qquad (9)$$

where $\Delta F^{\mathrm{clr}}_{\mathrm{LW}}$ is the LW DREA.

We use cloud fraction from the CERES cloud mask to estimate $\Delta F^{\mathrm{tot}}_{\mathrm{SW}}$ and $\Delta F(\lambda, \phi, d) = \overline{F}_{\mathrm{na}}(\lambda, \phi, d) - \overline{F}_a(\lambda, \phi, d)$ for NOAA SSF, and the MOD04 SSF cloud fraction parameter to estimate the corresponding quantities for MOD04. The MOD04 SSF cloud fraction parameter is determined by averaging the MOD04 "cloud fraction ocean" parameter in a CERES footprint, accounting for the CERES point-spread function. In MOD04 processing, all parameters, including the cloud fraction ocean parameter, are set to default if less than 20 MODIS pixels out of 400 in a 10 km $\times$ 10 km box (<5%) are determined to be cloud free (L. A. Remer 2004, personal communication). As a result, statistics from the MOD04 cloud fraction ocean parameter will miss purely overcast conditions. To obtain statistically representative cloud fraction information from the MOD04 SSF cloud fraction parameter, we assume that if a default cloud fraction occurs when more than 95% of the MODIS pixel radiances in a footprint are nondefault, the footprint is overcast. As a result, the MOD04 SSF cloud fraction will always overestimate cloud fraction. Another factor that contributes to its overestimation is the spatial variability test, which flags all pixels in a 3 $\times$ 3 pixel array as cloudy when the standard deviation threshold is exceeded, even if only a few pixels may, in fact, be cloudy.

Figure 16 provides the global annual average of $\Delta F^{\mathrm{clr}}_{\mathrm{SW}}$, $\Delta F^{\mathrm{tot}}_{\mathrm{SW}}$, and $\Delta F(\lambda, \phi, d) = \overline{F}_{\mathrm{na}}(\lambda, \phi, d) - \overline{F}_a(\lambda, \phi, d)$ over ocean for March 2000 through February 2001. The net total-sky DREA is negative (cooling) and ranges from -1.6 (NOAA SSF) to -2.0 (MOD04) W m^{-2}. Compared to $\Delta F^{\mathrm{clr}}_{\mathrm{SW}}$, $\Delta F^{\mathrm{tot}}_{\mathrm{SW}}$ is a factor of 2–2.5 smaller in magnitude, $\Delta F^{\mathrm{clr}}_{\mathrm{SW}}$ and $\Delta F^{\mathrm{tot}}_{\mathrm{SW}}$ differs from $\Delta F^{\mathrm{tot}}_{\mathrm{SW}}$ by <0.25 W m^{-2}. The global mean clear-area fraction that is derived from the CERES cloud mask is 0.311, compared to 0.192 from MOD04 SSF. Because of these differences, the clear and cloudy areas in the MOD04 analysis contribute approximately equally to the total-

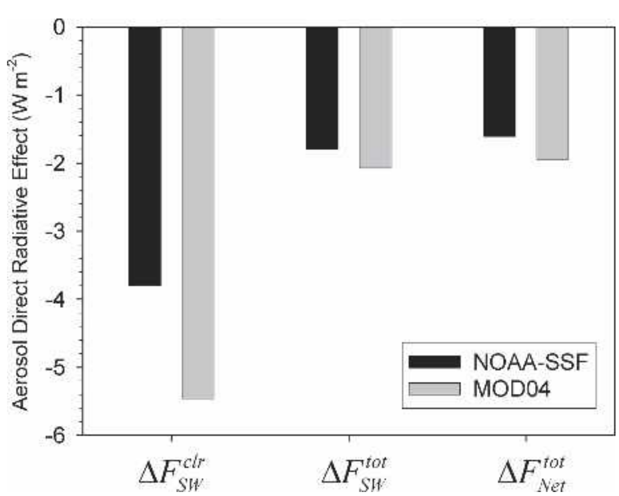

FIG. 16. Average clear-sky SW, total-sky SW, and total-sky net direct radiative effect of aerosols over global ocean from NOAA SSF and MOD04 for Mar 2000–Feb 2001.

TABLE 3. Clear-sky SW DREA (ΔF_{SW}^{clr}), total-sky SW DREA (ΔF_{SW}^{tot}), total-sky net DREA (ΔF_{Net}^{tot}), and average 0.644-μm aerosol optical depth (τ_a) inferred from NOAA SSF clear-sky radiances, and CERES clear fraction $(1 - f)$ determined from the CERES cloud mask for Mar–May 2000.

Region	ΔF_{SW}^{clr}	ΔF_{SW}^{tot}	ΔF_{Net}^{tot}	τ_a	$1 - f$
1	−6.24	−2.09	−1.94	0.173	0.184
2	−5.74	−2.25	−2.04	0.162	0.251
3	−7.85	−4.45	−3.97	0.215	0.449
4	−8.67	−2.84	−2.64	0.245	0.166
5	−3.89	−2.44	−2.07	0.158	0.468
6	−5.57	−3.42	−2.92	0.218	0.463
7	−6.37	−4.72	−3.98	0.242	0.618
8	−4.01	−2.25	−1.90	0.159	0.436
9	−3.03	−1.87	−1.64	0.096	0.476
10	−3.60	−2.22	−1.94	0.117	0.463
11	−3.58	−2.20	−1.93	0.114	0.478
12	−3.45	−1.82	−1.62	0.110	0.365
13	−3.57	−1.17	−1.10	0.084	0.180

sky SW DREA, while the NOAA SSF analysis with f inferred from the CERES cloud mask suggests that approximately 65% of the total-sky SW DREA is from clear areas and 35% is from cloudy areas.

A summary of these and the associated 0.644-μm aerosol optical depth and clear-sky fraction in each of the 13 regions in Fig. 10 are provided in Tables 3–10. The seasonal variation in $\Delta F(\lambda, \phi, d) = \overline{F}_{na}(\lambda, \phi, d) - \overline{F}_a(\lambda, \phi, d)$ depends strongly upon changes in $(1 - f)$. For example, in both NOAA SSF and MOD04, the largest seasonal changes in ΔF_{SW}^{clr} and 0.644-μm aerosol optical depth occur in region 4, but because $(1 - f)$ varies the most with season in region 3 (by 0.33), $\Delta F(\lambda, \phi, d) = \overline{F}_{na}(\lambda, \phi, d) - \overline{F}_a(\lambda, \phi, d)$ shows the largest seasonal variation in region 3, ranging from −1.9 W m^{-2} in DJF to −5.9 W m^{-2} in JJA based on MOD04, and from −2.0 to −4.9 W m^{-2} based on NOAA SSF. Region 9 shows the smallest seasonal variation, with $\Delta F(\lambda, \phi, d) = \overline{F}_{na}(\lambda, \phi, d) - \overline{F}_a(\lambda, \phi, d)$ varying by <0.35 W m^{-2} and $(1 - f)$ varying by <0.045.

TABLE 5. Same as Table 3, but for Sep–Nov 2000.

Region	ΔF_{SW}^{clr}	ΔF_{SW}^{tot}	ΔF_{Net}^{tot}	τ_a	$1 - f$
1	−3.98	−1.43	−1.30	0.108	0.236
2	−3.92	−1.59	−1.44	0.109	0.270
3	−6.49	−3.66	−3.27	0.177	0.435
4	−4.96	−1.82	−1.66	0.139	0.236
5	−2.84	−1.54	−1.32	0.114	0.389
6	−4.30	−2.53	−2.18	0.164	0.437
7	−5.17	−3.41	−2.91	0.202	0.500
8	−3.22	−1.75	−1.49	0.126	0.417
9	−2.61	−1.68	−1.40	0.113	0.512
10	−3.64	−1.88	−1.61	0.149	0.351
11	−3.92	−2.17	−1.84	0.158	0.421
12	−3.50	−2.17	−1.83	0.146	0.459
13	−4.74	−1.57	−1.46	0.123	0.181

Differences in the DREA from NOAA SSF and MOD04 also show a strong seasonal dependence. In general, the two are more consistent in September–November (SON) and DJF than they are in MAM and JJA. In the former seasons, differences in ΔF_{SW}^{clr} remain <2.2 W m^{-2}, and differences in $\Delta F(\lambda, \phi, d) = \overline{F}_{na}(\lambda, \phi, d) - \overline{F}_a(\lambda, \phi, d)$ remain <0.5 W m^{-2}. In MAM and JJA, differences in ΔF_{SW}^{clr} reach 5.5 W m^{-2} and differences in $\Delta F(\lambda, \phi, d) = \overline{F}_{na}(\lambda, \phi, d) - \overline{F}_a(\lambda, \phi, d)$ reach 2.1 W m^{-2}.

5. Summary and conclusions

The direct radiative effect of aerosols (DREA) under clear-sky conditions over ocean is estimated by exploiting the synergy between CERES and MODIS measurements on *Terra* to account for aerosol contributions at spatial scales that are smaller than those of the CERES footprints. MODIS CERES narrow-to-broadband regressions are used to convert clear-sky MODIS narrow-

TABLE 4. Same as Table 3, but for Jun–Aug 2000.

Region	ΔF_{SW}^{clr}	ΔF_{SW}^{tot}	ΔF_{Net}^{tot}	τ_a	$1 - f$
1	−3.53	−1.23	−1.13	0.105	0.198
2	−4.25	−2.02	−1.81	0.125	0.346
3	−7.45	−5.54	−4.86	0.209	0.651
4	−5.08	−1.91	−1.75	0.147	0.225
5	−3.07	−1.78	−1.54	0.116	0.409
6	−5.99	−3.59	−3.11	0.216	0.444
7	−8.34	−4.55	−4.06	0.300	0.325
8	−3.06	−1.64	−1.42	0.113	0.399
9	−2.95	−1.88	−1.67	0.086	0.485
10	−3.70	−2.03	−1.82	0.106	0.387
11	−4.45	−2.49	−2.24	0.125	0.407
12	−3.56	−2.06	−1.84	0.101	0.431
13	−2.63	−0.99	−0.93	0.067	0.189

TABLE 6. Same as Table 3, but for Dec 2000–Feb 2001.

Region	ΔF_{SW}^{clr}	ΔF_{SW}^{tot}	ΔF_{Net}^{tot}	τ_a	$1 - f$
1	−3.99	−1.23	−1.13	0.106	0.189
2	−4.20	−1.30	−1.20	0.113	0.173
3	−4.77	−2.17	−1.97	0.122	0.320
4	−6.04	−1.71	−1.59	0.161	0.146
5	−3.98	−2.19	−1.92	0.131	0.413
6	−6.28	−3.68	−3.22	0.205	0.443
7	−6.19	−4.32	−3.71	0.209	0.578
8	−5.04	−2.51	−2.23	0.160	0.350
9	−2.93	−1.90	−1.60	0.118	0.513
10	−3.71	−2.28	−1.94	0.145	0.473
11	−3.61	−2.07	−1.75	0.145	0.445
12	−3.62	−1.78	−1.54	0.144	0.324
13	−5.26	−1.77	−1.63	0.135	0.213

TABLE 7. Clear-sky SW DREA (ΔF_{SW}^{clr}), total-sky SW DREA (ΔF_{SW}^{tot}), total-sky net DREA (ΔF_{Net}^{tot}), and average 0.644-μm aerosol optical depth (τ_a) inferred from MOD04 clear-sky radiances, and CERES clear fraction ($1 - f$) determined from the MOD04 SSF cloud fraction for Mar–May 2000.

Region	ΔF_{SW}^{clr}	ΔF_{SW}^{tot}	ΔF_{Net}^{tot}	τ_a	$1 - f$
1	−9.26	−2.76	−2.55	0.230	0.125
2	−8.63	−2.92	−2.66	0.207	0.190
3	−10.58	−5.82	−5.24	0.263	0.370
4	−13.67	−4.15	−3.86	0.353	0.146
5	−4.90	−2.64	−2.29	0.150	0.298
6	−7.70	−4.36	−3.80	0.242	0.338
7	−8.05	−5.30	−4.53	0.252	0.463
8	−4.80	−2.25	−1.92	0.151	0.231
9	−3.34	−1.71	−1.50	0.090	0.269
10	−4.33	−2.26	−2.00	0.112	0.294
11	−4.07	−2.11	−1.86	0.107	0.285
12	−3.60	−1.62	−1.44	0.096	0.191
13	−4.88	−1.30	−1.20	0.110	0.117

TABLE 9. Same as Table 7, but for Sep–Nov 2000.

Region	ΔF_{SW}^{clr}	ΔF_{SW}^{tot}	ΔF_{Net}^{tot}	τ_a	$1 - f$
1	−5.13	−1.56	−1.42	0.124	0.149
2	−5.02	−1.73	−1.56	0.121	0.176
3	−7.20	−3.88	−3.52	0.164	0.345
4	−6.40	−2.05	−1.87	0.151	0.162
5	−3.70	−1.67	−1.47	0.104	0.220
6	−5.68	−2.86	−2.50	0.166	0.259
7	−6.75	−3.85	−3.37	0.195	0.340
8	−3.82	−1.68	−1.45	0.112	0.191
9	−3.57	−1.93	−1.68	0.099	0.311
10	−5.24	−2.35	−2.10	0.140	0.241
11	−5.42	−2.60	−2.27	0.154	0.265
12	−4.52	−2.36	−2.06	0.129	0.264
13	−6.93	−1.94	−1.80	0.158	0.126

band radiances to broadband shortwave (SW) radiances, and CERES clear-sky angular distribution models (ADMs) (Loeb et al. 2005) are used to estimate the corresponding top-of-atmosphere (TOA) radiative fluxes, from which the DREA is determined. The uncertainty in SW radiance from the narrow-to-broadband fits is approximately 2.75% after averaging over 1° latitude × 1° longitude regions, which corresponds to a 24-h-averaged regional SW TOA flux uncertainty of approximately 1 W m^{-2}. The sensitivity in the DREA to uncertainties in cloud screening is investigated by comparing the DREA obtained for regions that are identified as being clear by the NOAA/NESDIS aerosol algorithm (Ignatov and Stowe 2002) in the CERES SSF product (Ignatov et al. 2005) (NOAA SSF) with that obtained for clear regions in the MOD04 product (Remer et al. 2005). Both NOAA SSF and MOD04 use MODIS *Terra* measurements, but they rely on independent cloud screening algorithms. Regionally, differences are largest in regions where aerosol concentrations are largest. For example, in oceanic regions that are adjacent to the Sahara and Saudi Arabian deserts, the DREA from MOD04 exceeds that from NOAA SSF by up to 10 W m^{-2}. In northern Pacific Ocean regions that are affected by dust transported from Asia (mainly in June–August), DREA from MOD04 exceeds that from NOAA SSF by up to 35 W m^{-2}. Global radiative cooling by aerosols over ocean from MOD04 clear-sky radiances is −5.5 W m^{-2}, which is 1.7 W m^{-2} (44%) larger than that from NOAA SSF. The global annual average MOD04 DREA is within 0.06 W m^{-2} (1%) of that obtained from a study by Chou et al. (2002), who used SeaWiFS measurements for January–December 1998. Radiative cooling from MOD04 exceeds that of Chou et al.'s (2002) in the Northern Hemisphere (NH) by 0.65 W m^{-2}, reaching 2 W m^{-2} during the NH spring and summer, while radiative cooling in the Southern Hemisphere (SH) is more pronounced in Chou et al.'s (2002) study by 0.5 W m^{-2}.

TABLE 8. Same as Table 7, but for Jun–Aug 2000.

Region	ΔF_{SW}^{clr}	ΔF_{SW}^{tot}	ΔF_{Net}^{tot}	τ_a	$1 - f$
1	−8.01	−2.12	−1.92	0.204	0.132
2	−7.15	−2.79	−2.50	0.165	0.238
3	−9.09	−6.49	−5.85	0.196	0.562
4	−10.53	−3.19	−2.90	0.273	0.152
5	−4.12	−1.98	−1.75	0.113	0.230
6	−8.85	−4.75	−4.17	0.259	0.294
7	−12.41	−6.74	−6.13	0.382	0.292
8	−3.70	−1.59	−1.38	0.109	0.175
9	−3.55	−1.91	−1.69	0.092	0.312
10	−4.78	−2.29	−2.07	0.116	0.274
11	−5.43	−2.70	−2.41	0.140	0.277
12	−4.15	−2.02	−1.80	0.103	0.266
13	−3.07	−0.91	−0.82	0.089	0.092

TABLE 10. Same as Table 7, but for Dec 2000–Feb 2001.

Region	ΔF_{SW}^{clr}	ΔF_{SW}^{tot}	ΔF_{Net}^{tot}	τ_a	$1 - f$
1	−4.69	−1.21	−1.09	0.133	0.103
2	−4.70	−1.25	−1.14	0.126	0.111
3	−4.79	−2.09	−1.89	0.122	0.229
4	−6.76	−1.66	−1.53	0.177	0.104
5	−4.50	−2.11	−1.87	0.118	0.264
6	−7.47	−4.03	−3.58	0.205	0.334
7	−7.12	−4.44	−3.88	0.196	0.425
8	−5.25	−2.23	−1.99	0.138	0.202
9	−3.89	−2.04	−1.81	0.090	0.274
10	−5.04	−2.65	−2.36	0.121	0.299
11	−4.81	−2.30	−2.04	0.117	0.242
12	−4.29	−1.78	−1.61	0.103	0.151
13	−7.28	−2.10	−1.94	0.149	0.150

Aerosol optical depths from NOAA SSF and MOD04 both increase with the fractional cloud cover in a CERES footprint. While the exact reason for this increase is unclear, it likely the result of a combination of factors, including meteorology (wind speed and relative humidity) and cloud contamination. NOAA SSF aerosol optical depths are generally larger than those from MOD04, except when cloud cover—as determined from the CERES cloud mask—exceeds 95%. In that range of cloud cover, there is a sudden increase in MOD04 aerosol optical depths and their frequency of occurrence. When MOD04 aerosol retrievals occur in CERES footprints that are identified as being overcast by the CERES cloud mask, they are generally found in dust regions near the Sahara and Saudi Arabian Deserts. Clearly, more study is needed to reduce cloud screening uncertainties in regions of dust aerosol. Undoubtedly, high-resolution measurements from the Cloud-Aerosol Lidar and Infrared Pathfinder Satellite Observations (CALIPSO) (Winker et al. 2003) will be highly useful in resolving such differences among conventional cloud screening techniques.

Dust aerosols from deserts in northwestern China introduce a pronounced seasonal cycle in the DREA and aerosol optical depth over the northern Pacific Ocean between 30° and 60°N, with the strongest SW radiative cooling by aerosol occurring between March and April. In May 2003, the SW radiative cooling in the northwestern Pacific Ocean reaches 15.3 W m^{-2}. This corresponds to a 90% (7.3 W m^{-2}) increase compared to the average for that month from the previous 3 yr. Over the 4 yr of *Terra* data that are considered (March 2000–December 2003), the deseasonalized anomaly time series in the DREA shows no systematic trend in any of the regions considered.

Global ocean estimates of the total-sky SW DREA and net DREA at the TOA suffer from large uncertainties resulting from the lack of information on the vertical distribution of cloud and aerosol layers. Assuming that aerosol contributions in a cloudy column occur beneath the cloud layer, total-sky SW radiative cooling is estimated to be 2.0 W m^{-2}, roughly 2.75 times smaller than the magnitude of the clear-sky SW DREA. While a positive LW DREA is inferred when CERES LW fluxes are sorted by MODIS aerosol optical depth, the magnitude is highly variable owing to the lack of vertical information about the aerosol layer. Assuming representative values of aerosol LW radiative forcing efficiency over ocean, the global ocean total-sky net DREA is estimated to lie between 1.6 and 2.0 W m^{-2}.

We plan to extend the approach outlined in this study to also include estimates of the DREA over land surfaces where MODIS aerosol retrievals are available. Preliminary results suggest that narrow-to-broadband errors that are obtained by relating CERES SW radiances with MODIS radiances at 0.644, 0.858, and 1.632 μm are <3%.

Acknowledgments. This research was funded by the Clouds and the Earth's Radiant Energy System (CERES) project under NASA Grant NNL04AA26G and by Grant NNG04GM21G. The authors thank Professors James A. Coakley Jr., Robert J. Charlson, and Dr. Bruce A. Wielicki for the helpful discussions on this topic.

REFERENCES

Ackerman, A. S., O. B. Toon, D. E. Stevens, A. J. Heymsfield, V. Ramanathan, and E. J. Welton, 2000: Reduction of tropical cloudiness by soot. *Science,* **288,** 1042–1047.

Ackerman, S. A., K. I. Strabala, W. P. Menzel, R. A. Frey, C. C. Moeller, and L. E. Gumley, 1998: Discriminating clear sky from clouds with MODIS. *J. Geophys. Res.,* **103,** 32 139–32 140.

Barnes, W. L., T. S. Pagano, and V. V. Salomonson, 1998: Prelaunch characteristics of the Moderate Resolution Imaging Spectroradiometer (MODIS) on EOS-AM1. *IEEE Trans. Geosci. Remote Sens.,* **36,** 1088–1100.

Boucher, O., and D. Tanré, 2000: Estimation of the aerosol perturbation to the Earth's radiative budget over oceans using POLDER satellite aerosol retrievals. *Geophys. Res. Lett.,* **27,** 1103–1106.

Chou, M.-D., P.-K. Chan, and M. Wang, 2002: Aerosol radiative forcing derived from SeaWiFS-retrieved aerosol optical properties. *J. Atmos. Sci.,* **59,** 748–757.

Christopher, S. A., J. Chou, J. Zhang, X. Li, and R. M. Welch, 2000: Shortwave direct radiative forcing of biomass burning aerosols estimated from VIRS and CERES. *Geophys. Res. Lett.,* **27,** 2197–2200.

Clarke, A. D., and Coauthors, 2002: INDOEX aerosol: A comparison and summary of chemical, microphysical, and optical properties observed from land, ship, and aircraft. *J. Geophys. Res.,* **107,** 8033, doi:10.1029/2001JD000572.

Diner, D. J., and Coauthors, 2004: PARAGON: An integrated approach for characterizing aerosol climate impacts and environmental interactions. *Bull. Amer. Meteor. Soc.,* **85,** 1491–1501.

Gao, B.-C., Y. J. Kaufman, D. Tanré, and R.-R. Li, 2002: Distinguishing tropospheric aerosols from thin cirrus clouds for improved aerosol retrievals using the ratio of 1.38-μm and 1.24-μm channels. *Geophys. Res. Lett.,* **29,** 1890, doi:10.1029/2002GL015475.

Geier, E. B., R. N. Green, D. P. Kratz, P. Minnis, W. F. Miller, S. K. Nolan, and C. B. Franklin, cited 2001: Single satellite footprint TOA/surface fluxes and clouds (SSF) collection document. [Available online at http://asd-www.larc.nasa.gov/ceres/collect_guide/SSF_CG.pdf.]

Geogdzhayev, I. V., M. I. Mishchenko, L. Liu, and L. Remer, 2004: Global two-channel AVHRR aerosol climatology: Effects of stratospheric aerosols and preliminary comparisons with MODIS and MISR retrievals. *J. Quant. Spectrosc. Radiat. Tranfer,* **88,** 47–59.

Harrison, E. F., P. Minnis, B. R. Barkstrom, V. Ramanathan, R. D. Cess, and G. G. Gibson, 1990: Seasonal variations of cloud radiative forcing derived from the Earth Radiation Budget Experiment. *J. Geophys. Res.,* **95,** 18 687–18 703.

Haywood, J. M., V. Ramaswamy, and B. J. Soden, 1999: Tropospheric aerosol climate forcing in clear-sky satellite observations over the oceans. *Science,* **283,** 1299–1303.

Houghton, J. H., Y. Ding, D. J. Griggs, M. Noguer, P. J. van der Linden, X. Dai, K. Maskell, and C. A. Johnson, Eds., 2001: *Climate Change 2001: The Scientific Basis.* Cambridge University Press, 882 pp.

Ignatov, A., and L. L. Stowe, 2002: Aerosol retrievals from individual AVHRR channels: I. Retrieval algorithm and transition from Dave to 6S radiative transfer model. *J. Atmos. Sci.,* **59,** 313–334.

——, and Coauthors, 2005: Two MODIS aerosol products over ocean on the *Terra* and *Aqua* CERES SSF datasets. *J. Atmos. Sci.,* **62,** 1008–1031.

Kato, S., N. G. Loeb, and C. K. Rutledge, 2002: Estimate of top-of-atmosphere albedo for a molecular atmosphere over ocean using Clouds and the Earth's Radiant Energy System measurements. *J. Geophys. Res.,* **107,** 4396, doi:10.1029/2001JD001309.

Kiehl, J. T., and K. E. Trenberth, 1997: Earth's annual global mean energy budget. *Bull. Amer. Meteor. Soc.,* **78,** 197–208.

Kinne, S., and Coauthors, 2003: Monthly averages of aerosol properties: A global comparison among models, satellite data, and AERONET ground data. *J. Geophys. Res.,* **108,** 4634, doi:10.1029/2001JD001253.

Li, R.-R., Y. J. Kaufman, B.-C. Gao, and C. O. Davis, 2003: Remote sensing of suspended sediments and shallow coastal waters. *IEEE Trans. Geosci. Remote Sens.,* **41,** 559–566.

Li, X., S. A. Christopher, J. Chou, and R. M. Welch, 2000: Estimation of shortwave direct radiative forcing of biomass burning aerosols using angular dependence models. *J. Appl. Meteor.,* **39,** 2278–2291.

Liu, Z., M. A. Vaughan, D. M. Winker, C. A. Hostetler, L. R. Poole, D. Hlavka, W. Hart, and M. McGill, 2004: Use of probability functions for discriminating between cloud and aerosol in lidar backscatter data. *J. Geophys. Res.,* **109,** D15202, doi:10.1029/2004JD004732.

Loeb, N. G., and S. Kato, 2002: Top-of-atmosphere direct radiative effect of aerosols over the tropical oceans from the Clouds and the Earth's Radiant Energy System (CERES) satellite instrument. *J. Climate,* **15,** 1474–1484.

——, N. M. Smith, S. Kato, W. F. Miller, S. K. Gupta, P. Minnis, and B. A. Wielicki, 2003: Angular distribution models for top-of-atmosphere radiative flux estimation from the Clouds and the Earth's Radiant Energy System instrument on the Tropical Rainfall Measuring Mission Satellite. Part I: Methodology. *J. Appl. Meteor.,* **42,** 240–265.

——, S. Kato, K. Loukachine, and N. M. Smith, 2005: Angular distribution models for top-of-atmosphere radiative flux estimation from the Clouds and the Earth's Radiant Energy System instrument on the *Terra* satellite. Part I: Methodology. *J. Atmos. Oceanic Technol.,* **22,** 338–351.

Martins, J. V., D. Tanré, L. Remer, Y. Kaufman, S. Mattoo, and R. Levy, 2002: MODIS cloud screening for remote sensing of aerosol over oceans using spatial variability. *Geophys. Res. Lett.,* **29,** 8009, doi:10.1029/2001GL013252.

Minnis, P., D. F. Young, S. Sun-Mack, P. W. Heck, D. R. Doelling, and Q. Trepte, 2003: CERES cloud property retrievals from imagers on *TRMM, Terra*, and Aqua. *Proc. SPIE 10th Int. Symp. on Remote Sensing: Conf. on Remote Sensing of Clouds and the Atmosphere VII*, Barcelona, Spain, SPIE, 37–48.

Rajeev, K., S. K. Nair, K. Parameswaran, and C. S. Raju, 2004: Satellite observations of the regional aerosol distribution and transport over the Arabian Sea, Bay of Bengal and Indian Ocean. *Indian J. Mar. Sci.,* **33,** 30–39.

Remer, L. A., and Coauthors, 2005: The MODIS aerosol algorithm, products, and validation. *J. Atmos. Sci.,* **62,** 947–973.

Satheesh, S. K., and D. Lubin, 2003: Short wave versus long wave radiative forcing by Indian Ocean aerosols: Role of sea-surface winds. *Geophys. Res. Lett.,* **30,** 1695, doi:10.1029/2003GL017499.

——, V. Ramanathan, X. Li-Jones, J. M. Lobert, I. A. Podgorny, J. M. Prospero, B. N. Holben, and N. G. Loeb, 1999: A model for the natural and anthropogenic aerosols over the tropical Indian Ocean derived from INDOEX data. *J. Geophys. Res.,* **104,** 27 421–27 440.

Smith, G. L., 1994: Effects of time response on the point spread function of a scanning radiometer. *Appl. Opt.,* **33,** 7031–7037.

Stowe, L. L., P. A. Davis, and E. P. McClain, 1999: Scientific basis and initial evaluation of the CLAVR-1 global clear/cloud classification algorithm for the Advanced Very High Resolution Radiometer. *J. Atmos. Oceanic Technol.,* **16,** 656–681.

Suarez, M. J., and Coauthors, 2005: Documentation and validation of the Goddard Earth Observing System (GEOS) data assimilation system—Version 4. NASA Tech. Series on Global Modeling and Data Assimilation, NASA/TM-2005-104606, Vol. 26, Goddard Space Flight Center, 165 pp.

Tanré, D., M. Herman, and Y. J. Kaufman, 1996: Information on aerosol size distribution contained in solar reflected spectral radiances. *J. Geophys. Res.,* **101,** 19 043–19 060.

Trepte, Q., Y. Chen, S. Sun-Mack, P. Minnis, D. F. Young, B. A. Baum, and P. W. Heck, 1999: Scene identification for the CERES cloud analysis subsystem. Preprints, *10th Conf. on Atmospheric Radiation,* Madison, WI, Amer. Meteor. Soc., 169–172.

Weaver, C. J., P. Ginoux, N. C. Hsu, M.-D. Chou, and J. Joiner, 2002: Radiative forcing of Saharan Dust: GOCART model simulations compared with ERBE data. *J. Atmos. Sci.,* **59,** 736–747.

Winker, D. M., J. R. Pelon, and M. P. McCormick, 2003: The CALIPSO mission: Spaceborne lidar for observation of aerosols and clouds. *Proc. SPIE Int. Soc. Opt. Eng.,* **4893,** 1–11.

Young, D. F., P. Minnis, D. R. Doelling, G. G. Gibson, and T. Wong, 1998: Temporal interpolation methods for the Clouds and the Earth's Radiant Energy System (CERES) experiment. *J. Appl. Meteor.,* **37,** 572–590.

Zhang, J., and S. A. Christopher, 2003: Longwave radiative forcing of Saharan dust aerosols estimated from MODIS, MISR, and CERES observations on Terra. *Geophys. Res. Lett.,* **30,** 2188, doi:10.1029/2003GL018479.